https://doi.org/10.5194/egusphere-2025-6249
Preprint. Discussion started: 21 January 2026

Towards the Bayesian calibration of a glacier surface energy balance model for unmonitored glaciers

Jan Niklas Richter[1], Anselm Arndt[2], Nikolina Ban[1], Nicolas Gampierakis[1,3], Fabien Maussion[1,3], Rainer Prinz[1], Matthias Scheiter[4,5], Nikolaus Umlauf[6], and Lindsey Nicholson[1]

[1]Department of Atmospheric and Cryospheric Sciences, University of Innsbruck, Innsbruck, Austria
[2]Geography Department, Humboldt-Universität zu Berlin, Berlin, Germany
[3]School of Geographical Sciences, University of Bristol, Bristol, UK
[4]Australian Centre for Excellence in Antarctic Science, University of Tasmania, Hobart, Tasmania, Australia
[5]Laboratoire de Glaciologie, Université libre de Bruxelles, Brussels, Belgium
[6]Department of Statistics, University of Innsbruck, Innsbruck, Austria

Correspondence: Jan Niklas Richter (niklas.richter@student.uibk.ac.at)

Abstract. Building on Bayesian calibration techniques and leveraging high-resolution climate simulations, we test the current capabilities of calibrating a surface energy balance model for unmonitored glaciers using only globally available satellite observations at Hintereisferner. We developed a multi-objective Bayesian framework for the Coupled Snowpack and Ice surface energy and mass balance model in Python (COSIPY), calibrated with satellite-derived geodetic mass balance, transient snowline altitudes, and mean glacier albedo. The framework is evaluated with in-situ observations and weather station measurements. A Latin Hypercube Sampling ensemble was used to investigate the model's parameter behaviour, establish priors and enable a Markov Chain Monte Carlo calibration helped by a novel and computationally efficient COSIPY emulator. The multi-objective calibration successfully constrains parameter distributions, addressing the equifinality between accumulation and albedo parameters. However, tighter parameter constraints, combined with imperfect climate simulations as forcing, create a model solution that requires a compromise between the three observational targets. Model evaluation shows that the calibrated ensemble reproduces glacier-mean albedos and inter-annual mass-balance variability well, but exhibits a negative bias in mean annual mass balance and a delayed snowline rise. This apparent contradiction arises from both forcing and model limitations. Incoming longwave radiation is overestimated throughout the year, while a warm and humid bias in the meteorological input during the later melt season enhances the positive turbulent fluxes. Early season melt is delayed by underestimated incoming shortwave radiation, and by an overly slow albedo decay caused by too high albedo aging and firn albedo parameters. Such biases in the meteorological forcing data remain a major obstacle to applying surface energy balance models to unmonitored glaciers. The calibration framework presented in this study provides diagnostic tools that help identify shortcomings and compensation effects within the modelling chain, paving the way for correcting forcing biases within a Bayesian framework as more observations become available. The open-source tools developed here have the potential to lower the barrier to studying the atmospheric drivers of glacier change at unmonitored sites with explicit treatment of uncertainty.

https://doi.org/10.5194/egusphere-2025-6249
Preprint. Discussion started: 21 January 2026

1 Introduction

Glaciers react to ambient atmospheric conditions via surface energy and mass exchanges at the glacier-atmosphere interface and are thus pivotal indicators of ongoing and past climatic changes (Oerlemans, 2001; Haeberli et al., 2007; Roe et al., 2017). Between 2000 and 2023, global glacier mass loss totalled 273 ± 16 gigatonnes per year, with the loss accelerating over time (Hugonnet et al., 2021; The GlaMBIE Team et al., 2025). This mass loss invokes cascading consequences that can affect global sea level rise (e.g., Zemp et al., 2019; Frederikse et al., 2020), regional freshwater availability (Ultee et al., 2022; Aguayo et al., 2024), hydro-political conflicts, diminishing eco-system services (e.g., Cook et al., 2021; Nie et al., 2021) and local hazards (e.g., GAPHAZ, 2017; Shugar et al., 2021; Furian et al., 2022). Given the societal and environmental impacts, the ability to accurately project future glacier evolution is crucial.

To address this need, researchers have developed a suite of numerical glacier models, coordinating their efforts at regional to global scales through three iterations of the Glacier Model Intercomparison Project (Glacier-MIP; e.g., Hock et al., 2019). These models mostly rely on the temperature-index (TI) method (Hock, 2003), which requires minimal data inputs and can adequately simulate glacier snow and ice melt when air temperature is well correlated to the melt energy or its driver (Ohmura, 2001; Sicart et al., 2008). However, the performance of TI models can be questioned under climatic conditions where this core assumption is violated and melt becomes highly non-linear (Marzeion et al., 2012; Litt et al., 2019). Most importantly, the TI method suffers from stationarity, as the degree-day factor is expected to change and cannot be constrained under a changing climate (Hock, 2003; Ismail et al., 2023; Silwal et al., 2023).

In contrast, surface energy (SEB) and mass balance (MB) models (e.g., Hock and Holmgren, 2005) do not inherently suffer from the stationarity assumption due to their physical basis (MacDougall et al., 2011). However, this assumption is violated, as the parameterisations used within these models often introduce a stationary parameter choice that is subject to the calibration data and period (Prinz et al., 2016; Galos et al., 2017; Zolles et al., 2019) and may change under a future climate as the glacier's environment changes (Oerlemans et al., 2009; Abermann et al., 2014; Zhang et al., 2021; Zolles and Born, 2021). Additionally, while traditionally calibrated for a single optimal parameter set, these models also exhibit the potential for equifinality, i.e. multiple equally well-fitting solutions (Rye et al., 2012; Zolles et al., 2019; Arndt and Schneider, 2023).

The primary limitation for applying SEB models however remains their high demand for in-situ observations, which are needed to constrain numerous tunable parameters and provide high-quality forcing data (Mölg et al., 2012; Gabbi et al., 2014; Réveillet et al., 2018). Only a few glaciers have in-situ observations to address this demand (Zemp et al., 2015), but tuned parameters are not directly transferable to other glaciers (Gurgiser et al., 2013; Zolles et al., 2019), while calibrating to regional mass balance averages leads to significant uncertainties and inaccuracies at the glacier level (Temme et al., 2023; Zekollari et al., 2024). Therefore, SEB models currently represent only three out of the 17 glacier evolution models employed throughout phases one to three of Glacier-MIP (Hock et al., 2019; Marzeion et al., 2020; Zekollari et al., 2025). The few regional-scale SEB applications, in turn, are often forced using coarse reanalysis data and calibrated assuming transferable parameters (Sakai and Fujita,

https://doi.org/10.5194/egusphere-2025-6249
Preprint. Discussion started: 21 January 2026

2017; Shannon et al., 2019; Temme et al., 2023; Mackay et al., 2025).

Satellite-derived geodetic mass balance estimates (Hugonnet et al., 2021) present in many cases the only direct mass change observation at the glacier level. While they enabled the calibration of TI-based glacier evolution models (e.g., Rounce et al., 2023; Zekollari et al., 2024), their temporal resolution is limited as a consequence of the signal-to-noise ratio in the change signal and the uncertainties in the density assumptions (Huss, 2013; Berthier et al., 2023). Therefore, they offer only limited information and give rise to equifinality problems (e.g., Rounce et al., 2020; Schuster et al., 2023).

In the absence of adequate in-situ measurements, the growing body of remotely available observations, including transient snow-cover data (Rastner et al., 2019; Racoviteanu et al., 2019; Loibl et al., 2025) and glacier albedo (Brun et al., 2015; Naegeli et al., 2019; Ren et al., 2024), offer a promising alternative to calibrate (glacier) models (e.g., Sirguey et al., 2016; Rabatel et al., 2017; Barandun et al., 2018; Williamson et al., 2020; Cremona et al., 2025). The integration of these observations into models has been enabled by recent advances in data assimilation techniques tailored for glaciology (Dumont et al., 2012; Landmann et al., 2021; Morlighem and Goldberg, 2023).

Concurrently, there has been significant progress in high-resolution and convection-permitting climate modelling (CPM; e.g., Collier et al., 2013; Bonekamp et al., 2019; Coppola et al., 2020; Mott et al., 2023), relevant process understanding (Voordendag et al., 2024; Quéno et al., 2024; Saigger et al., 2024) and downscaling (e.g., Reynolds et al., 2023). CPMs have shown an improved representation of various precipitation-related metrics (e.g., Ban et al., 2021; Li et al., 2021) and their uncertainties (Fosser et al., 2024). These models offer a promising avenue as meteorological forcing for SEB models where in situ measurements are sparse (Blau et al., 2021; Mackay et al., 2025; Ing et al., 2025). This is reflected in the portrayed added value for to snow cover (Lüthi et al., 2019; Gao et al., 2020) and snowpack simulations (e.g., Vionnet et al., 2019; He et al., 2019; Havens et al., 2019), air temperature and wind fields (Ma et al., 2023), clouds and top-of-atmosphere radiation budget (Hentgen et al., 2019).

Building on the pioneering calibrational framework for TI models established by Rounce et al. (2020) and Sjursen et al. (2023, 2025) and capitalising on a recent suite of CPM simulations at 2.2 km grid spacing (Leutwyler et al., 2017; Ban et al., 2020), we explore the applicability of a Bayesian parameter calibration scheme to the open-source COupled Snowpack and Ice surface energy and mass balance model in PYthon (COSIPY; Sauter et al., 2020). We synthesise these and globally available remotely-sensed glacier observations with the following aims:

1. Develop a calibration scheme for a physically-based SEB model where in-situ data are absent

2. Diagnose the sources of parameter equifinality within the model and assess the parametric uncertainty

3. Evaluate the resultant SEB simulations and the consequences of using this "remote-only" application in terms of forcing and parametric accuracy

This work presents, to our knowledge, the first application of recent advances in both glacier model calibration and climate modelling to a physically-based SEB model. Our goal is to critically assess our current capabilities towards a remote-only application of glacier SEB modelling, and we expect this relevance to grow in parallel with future improvements in glacier

https://doi.org/10.5194/egusphere-2025-6249
Preprint. Discussion started: 21 January 2026

observations and forcing data. We test our method at a well-studied glacier site in order to enable the comparison of the output of our workflow with more traditional applications of SEB models using high quality in situ data.

2 Methods and Data

Within this study, we built a Bayesian calibration framework to calibrate an established SEB model using only globally available remotely sensed data, while explicitly accounting for the uncertainty in these satellite products. This section first describes the SEB model and the meteorological and calibration datasets, before addressing the employed calibration framework and its evaluation against available automatic weather station (AWS) measurements and glaciological observations. We tested this workflow at the well-monitored Hintereisferner (HEF), a valley glacier in the Austrian Alps (Fig. 1), which is one of the world's reference glaciers recognised by the World Glacier Monitoring Service (WGMS, 2024), with continuous mass balance measurements since 1952/1953 (Kuhn et al., 1999; Strasser et al., 2018) as well as numerous additional meteorological and glaciological studies (e.g., Dirmhirn and Trojer, 1955; Kuhn et al., 1999; Klug et al., 2018; Mott et al., 2020; Goger et al., 2022; Voordendag et al., 2024).

2.1 COSIPY Model

The COSIPY model (Sauter et al., 2020) is a physically based, medium complexity glacier SEB model that can be accessed freely on GitHub (https://github.com/cryotools/cosipy, last accessed: 25.07.25). It is optimised for computational performance using High-Performance Computing Clusters and builds on a one-dimensional column-style architecture, allowing for fast parallelisation at scalable temporal and spatial resolutions. The model excludes basal processes and lateral exchanges of energy and mass between grid cells.

COSIPY is based on the conservation of mass and energy and combines the SEB with an adaptive, multi-layered subsurface scheme. In COSIPY, the SEB is defined at an infinitesimally thin skin layer as follows:

$$Q_{\mathrm{M}} = Q_{\mathrm{SWin}}(1-\alpha) + Q_{\mathrm{LWin}} + Q_{\mathrm{LWout}} + Q_{\mathrm{H}} + Q_{\mathrm{E}} + Q_{\mathrm{G}} + Q_{\mathrm{R}}, \tag{1}$$

where Q_{M} denotes available melt energy, Q_{SWin} incoming shortwave radiation, α surface albedo, Q_{LWin} and Q_{LWout} incoming and outgoing longwave radiation, Q_{H} sensible heat flux, Q_{E} latent heat flux, Q_{G} glacier heat flux and Q_{R} the sensible heat flux of rain, with fluxes towards the surface being taken as positive. The SEB is solved iteratively using an optimisation algorithm aimed at minimising the residual of equation 1. Except for Q_{SWin}, α and Q_{LWin}, all terms of Equation 1 are dependent on the surface temperature T_{s}, which constitutes the upper boundary condition to the heat equation of the subsurface. The surface and subsurface are thus linked through T_{s} and percolating surface melt and rain.

Turbulent fluxes were calculated using a bulk approach (see Sauter et al., 2020) assuming SEB closure (Van Tiggelen et al., 2024) and applying a stability correction based on the Monin–Obukhov similarity theory in favour of the bulk-Richardson number approximation (Lapo et al., 2015; Fitzpatrick et al., 2017). Since T_{s} is bounded by the melting point, any surplus energy from the SEB that would increase T_{s} beyond the melting point is redirected as melting energy. Similarly, a small

https://doi.org/10.5194/egusphere-2025-6249
Preprint. Discussion started: 21 January 2026

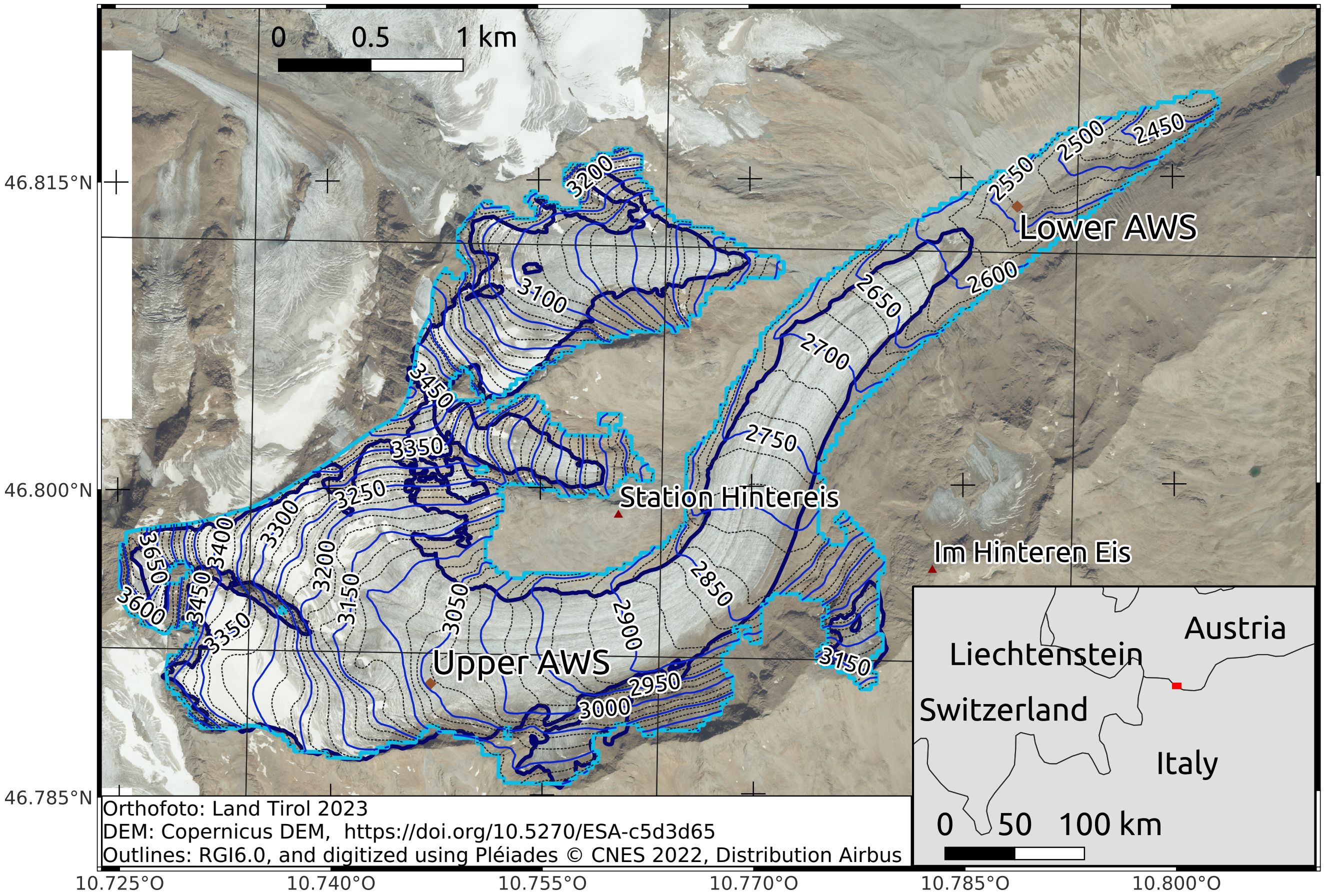

Figure 1. Map of the study area including the location of the available automatic weather stations (Upper AWS and Lower AWS), present-day reference stations (Station Hintereis and Im Hinteren Eis), manually digitised outlines based on the Pléiades Glacier Observatory imagery acquired in August 2022 (dark blue) and the Randolph Glacier Inventory version 6.0 outlines from 2003 (light blue) used within this study. The grid lines correspond to the COSMO grid at 2.2 km grid spacing. The background image was provided by the Land Tirol (data.tirol.gv.at) and the contour lines derived from Copernicus WorldDEM-30 (©DLR e.V. 2010 to 2014; ©Airbus Defence and Space GmbH 2014 to 2018), available under the Copernicus Programme (https://doi.org/10.5270/ESA-c5d3d65).

percentage (10 to 20%) of Q_{SWin} penetrates the subsurface following Bintanja and Van Den Broeke (1995), which can result in subsurface melting if the additional energy input would warm the subsurface layers beyond the melting point. As COSIPY neglects basal processes, the calculated mass balance is defined as the climatic mass balance (Cogley et al., 2011):

$$b_{\mathrm{clim}} = c_{\mathrm{sfc}} + a_{\mathrm{sfc}} + c_{\mathrm{i}} + a_{\mathrm{i}}. \tag{2}$$

Then surface accumulation c_{sfc} is the sum of accumulated snowfall and deposition of water vapour, while surface ablation a_{sfc} is the result of surface melt and sublimation. Refreezing can lead to internal accumulation c_{i}, and internal ablation a_{i} is the result of subsurface melting.

The model uses parameterisations for the fresh snow density (Vionnet et al., 2012), snow densification (Essery et al., 2013) and the temperature-dependent rain and snow partitioning (Hantel et al., 2000) when only total precipitation is provided. The parameterisation defines the fraction of precipitation falling as snow f_{snow} based on the near-surface air temperature at two meters T_2 as:

$$f_{\text{snow}} = 0.5\left(1 - \tanh\left(s_{\text{p}}\left(T_2 - T_{\text{rs}}\right)\right)\right). \tag{3}$$

This parameterisation introduces two parameters: the central temperature at which 50% of the total precipitation is solid T_{rs} and the spread parameter s_{p} which influences the transition between the two phases. Surface roughness is approximated based on surface facies and is set either constant when ice-covered or, in the case of snow or firn, linearly evolves from the prescribed fresh snow roughness to the roughness of firn (Mölg et al., 2009, 2012). The snow albedo α_{snow} is parameterised after Oerlemans and Knap (1998):

$$\alpha_{\text{snow}} = \alpha_{\text{firn}} + (\alpha_{\text{fs}} - \alpha_{\text{firn}})\exp\left(-\frac{s}{\alpha_{\text{aging}}}\right), \tag{4}$$

where α_{fs} is the constant fresh snow albedo and α_{firn} is the constant firn albedo. The constant albedo time scale α_{aging} describes how fast the snow albedo decays based on the time since the last snowfall s. In a consecutive step, the scheme accounts for snow thickness d:

$$\alpha = \alpha_{\text{snow}} + (\alpha_{\text{ice}} - \alpha_{\text{snow}})\exp\left(\frac{-d}{\alpha_{\text{depth}}}\right), \tag{5}$$

with the constant albedo of ice α_{ice} and the snow depth scale α_{depth}. COSIPY's modular structure allows for a fast implementation of additional parameterisation, depending on the user's needs (Gastaldello et al., 2025).

The model does not account for debris-covered surfaces or processes associated with snow redistribution and does not resolve ice dynamics. For a detailed description of the model, please refer to Sauter et al. (2020). In this manuscript, we utilise a customized version of the recent COSIPYv2.0.2 (Richter, 2025) adapted to employ the ray-tracing shortwave radiation correction scheme that accounts for both terrain- and self-shading (HORAYZON; Steger et al., 2022) and modified to calculate the modelled snowline altitudes (SLAs). We calculate the modelled SLA by first converting COSIPY's snowheight field to daily means and then taking the mean between maximum ice- and minimum snow-covered elevation defined with a minimum snow depth of 0.1 mm. If the glacier is fully snow-covered, the value is instead set to the minimum glacier elevation, and if it is entirely snow-free, it is set to the maximum glacier elevation.

2.2 Meteorological and static glacier forcing data

In this study, we used 2.2 km grid spacing convection-permitting Consortium for Small-scale Modelling - Climate Limited-area Modelling Community (COSMO-CLM; Rockel et al., 2008; Baldauf et al., 2011) simulations produced as part of the World Climate Research Programme sponsored Coordinated Regional Climate Downscaling Experiment (CORDEX) Flagship Pilot Study on convection over Europe and the Mediterranean (Coppola et al., 2020) and conducted by the ETH Zurich (Leutwyler et al., 2017; Ban et al., 2021). The simulations cover January 1999 to 2010 and are the result of a two-step, one-way nesting approach, with the boundary and initial conditions for the larger 12 km grid spacing domain provided by ERA-Interim (Dee et al., 2011) at six-hourly timesteps. For a detailed description of the simulations, see Leutwyler et al. (2017).

Forcing COSIPY requires hourly fields of near surface air temperature (T_2), relative humidity, wind speed, air pressure, total precipitation and snowfall (optional), incoming shortwave- and longwave radiation (Q_{SWin} and Q_{LWin}) or in the absence of the latter, total cloud cover fraction. Except for snowfall (daily), air pressure (6 hourly) and incoming long wave radiation (not available), we obtained all fields at hourly resolution directly from the Earth System Grid Federation (ESGF; https://esgf-ui.ceda.ac.uk/search, last accessed: 04.11.2025). Hourly air pressure fields are derived by linearly interpolating the six-hourly pressure fields.

We identified frequent mismatches in the snowfall and total precipitation fields and corrected a singular outlier at the end of March 2005, with a total precipitation value of more than 150 mm, by replacing it with the average of the surrounding two hourly timesteps. Instead of relying on the daily snowfall field, we derive hourly snowfall from hourly total precipitation using the temperature-based precipitation partitioning function (see Equation 3). We keep s_{p} at its default value of 1.0 °C and set T_{rs} to 1.55 °C which is similar to the value employed in other studies (e.g., Huss and Hock, 2015) and based on the analysis of Jennings et al. (2018).

We calculate two-meter wind speed assuming a logarithmic wind profile and a roughness length of 2.12 mm, based on the mean of the aerodynamic roughness length for firn and snow (Brock et al., 2006; Gromke et al., 2011; Arndt et al., 2021).

We applied lapse rates for relative humidity, T_2, total precipitation and snowfall to distribute the forcing data over the glacier surface, and extrapolated surface pressure with the barometric formula. We used the horizontal grid to derive local lapse rates over a three-by-three stencil located over the glacier centroid, due to the large spacing between vertically stored levels in the stored COSMO simulation at the standard pressure levels. Hourly lapse rates were calculated not to suppress small-scale and mesoscale interactions in the original COSMO-grid (Mölg and Kaser, 2011) and to allow for robust temporal variability. The resultant lapse rates are thus the product of a nine-sample linear regression. We chose this size since a comparison to a larger five-by-five stencil revealed only minor differences, and land surface types in COSMO-CLM and north-south divide effects remained consistent (Quéno et al., 2016; Vionnet et al., 2016). Similar to Buri et al. (2024), lapse rates were only applied when the elevation dependence exceeded a coefficient of determination R^2 of 0.7. Otherwise, they were set to zero or for temperature the environmental lapse rate of -6.5 K km^{-1}.

Finally, incoming longwave radiation was calculated based on the Stefan-Boltzmann law:

$$Q_{\mathrm{LWin}} = \epsilon_{\mathrm{a}}\, \sigma T_2^4, \tag{6}$$

where σ is the Stefan–Boltzmann constant and ϵ_a the atmospheric emissivity. We followed the formulation implemented in COSIPY, which combines the parameterisation of Konzelmann et al. (1994) with optimised parameters from Klok and Oerlemans (2002) to calculate ϵ_a based on fractional cloud cover n:

$$\epsilon_{\mathrm{a}} = \epsilon_{\mathrm{cs}}(1 - n^p) + \epsilon_{\mathrm{cl}} n^p. \tag{7}$$

https://doi.org/10.5194/egusphere-2025-6249
Preprint. Discussion started: 21 January 2026

In COSIPY, p is set to two (Greuell et al., 1997), ϵ_{cl} is the emissivity of clouds (set to 0.984; Klok and Oerlemans, 2002), and ϵ_{cs} denotes the clear-sky emissivity, given by:

$$\epsilon_{\mathrm{cs}} = 0.23 + b(e_2/T_2)^{1/8}, \tag{8}$$

where b is set to 0.433 (Klok and Oerlemans, 2002), T_2 is the air temperature at two meters and e_2 the water vapour pressure (Klok and Oerlemans, 2002).

Since most forcing fields are extrapolated using lapse rates, we applied a 20 m elevation band setup in COSIPY by averaging the shortwave correction factors generated from HORAYZON at each grid cell of the one-arcsecond resolution NASADEM (NASA JPL, 2020, last accessed: 19.03.2025).

To represent the glacier state during the time of the COSMO data availability, we used the glacier outlines from version 6.0 of the Randolph Glacier Inventory (RGI; RGI Consortium, 2017) dated to 2003 and representing a glacier extent of 8.04 km^2. In this study, we assume the glacier geometry to be unchanging over time, though we note the glacier has undergone continuous recession since the mid-20th century and in recent years (Fig. 1). We initialised the model in January 1999 with snow height simulated by the COSMO model and discarded the first year as spin-up in all further steps. We set the lower boundary condition for the subsurface temperature to 270.16 K and appointed an ice thickness of 191 m (Farinotti et al., 2019). This ensures numerical stability by preventing complete grid cell melt-out, which can occur under unrealistic parameter combinations.

2.3 Calibration data

We obtain the annual average specific mass change rate and its uncertainty of -1.0425 $\pm$ 0.261 meters water-equivalent per year (m w.e. a^{-1}) at HEF for the years 2000 to 2010 from the geodetic dataset of Hugonnet et al. (2021). Henceforth, we will report these values with two floating-point precision to improve readability. When comparing the observed and modelled mass balances, we loosely refer to both as B_{geod}, despite the fundamental differences between the two sources. While COSIPY simulates the climatic mass balance and thus ignores the typically one order of magnitude lower basal processes, these are inherently included in the geodetic mass balance. For more details, we refer the reader to Hugonnet et al. (2021).

While B_{geod} provides an integral calibration target, the temporal information remains limited. To address this gap, we employ transient SLA observations, derived from the Mountain Glacier Transient snowline Retrieval Algorithm (MANTRA; Loibl, 2023; Loibl et al., 2025) and glacier-averaged albedo $\bar{\alpha}$ as additional calibration targets.

The SLA values are computed from calibrated top-of-atmosphere Landsat data as the median of the lowest two elevation bands classified as snow-covered, and uncertainties are provided by the band's standard deviation. We refer the reader to Loibl et al. (2025) for further information. This calculation has two limitations. First, the measured SLA under fully snow-covered conditions does not directly reflect the glacier's minimum elevation. Second, cloud cover or terrain shading cannot be fully corrected for. This is especially relevant when cloud cover obstructs the glacier tongue and the SLA may be falsely classified on the cloud-free section. We corrected for the mismatch between minimum glacier elevation and SLA values on fully snow-covered days and manually filtered 21 misclassified scenes. As the uncertainties provided by the standard deviation can be very small, we set the minimum standard deviation to 20 m, which corresponds to the size of the elevation bands in COSIPY.

https://doi.org/10.5194/egusphere-2025-6249
Preprint. Discussion started: 21 January 2026

In addition, we derived remotely-sensed Landsat 5 and 7 per-pixel albedo measurements through the Google Earth Engine (Gorelick et al., 2017) following the anisotropy correction of Ren et al. (2021). In the first step, we applied terrain- and self-shading, combining the methods applied in Loibl et al. (2025) and in HORAYZON (Steger et al., 2022) based on the NASADEM. Next, we grouped all albedo pixel values into winter (DJFM) and summer (JJAS) seasons. We deleted values that extended beyond published ranges to mitigate the influence of potential outliers caused by sensor issues and filtered the data based on the second and 98th percentiles for each season. To provide information on likely albedo parameter ranges, we assumed that the α_{fs} must be in the upper 50% of observed values, giving a range of 0.887 to 0.93. Similarly, α_{ice} and α_{firn} should be in the lower 50% of observed values, ranging from 0.115 to 0.233 and 0.506 to 0.692, respectively (see Fig. S7 to S9).

Next, we derived $\bar{\alpha}$ as a third calibration target. Using all available scenes with a cloud cover less than 30%, we considered individual Landsat pixels to be correlated up to a radial distance L_{corr} of 500 m as assuming spatial independence results in unrealistically small uncertainties. Next, we estimated the number of effective samples N_{eff} using this correlation length as:

$$N_{\mathrm{eff}} = \frac{A_{\mathrm{total}}}{\pi {L_{\mathrm{corr}}}^2}, \tag{9}$$

where A_{total} is the summed area of all valid glacier pixels per scene. We adopted a constant per-pixel standard error σ^{sys} of 0.017 from Ren et al. (2021) to further account for sensor errors. The total uncertainty in glacier albedo was then estimated as:

$$\sigma_i^{\mathrm{alb}} = \sqrt{\left(\frac{\sigma_i^{\mathrm{spatial}}}{\sqrt{N_{\mathrm{eff}}}}\right)^2 + (\sigma^{\mathrm{sys}})^2} \tag{10}$$

where $\sigma_i^{\mathrm{spatial}}$ is the spatial standard deviation at each time step. The resulting uncertainty matches those estimated by Fugazza et al. (2016).

2.4 Parameter calibration and uncertainty analysis

To calibrate COSIPY at unmonitored sites using only globally available remote sensing data, we employed a Bayesian framework to account for the uncertainties inherent in these observational products. This approach was implemented using a Markov Chain Monte Carlo (MCMC) sampler to derive the full posterior probability distribution for each model parameter (Section 2.4.1). When considering unmonitored glaciers, a key challenge is defining informative prior distributions, which must be sensibly constrained for the site of interest. We addressed this by first conducting a sensitivity analysis and Latin Hypercube Sampling (LHS; McKay et al., 1979) of the parameter space to constrain the parameter choices and plausible parameter range. The resulting parameter space is then further investigated in detail regarding the model's parameter behaviour and the provided parameter constraints based on each observational dataset (Section 2.4.2). Finally, because MCMC methods require a large number of otherwise computationally intractable simulations, we developed a surrogate model to emulate COSIPY's outputs, ensuring the computational feasibility of the calibration scheme (Section 2.4.3).

https://doi.org/10.5194/egusphere-2025-6249
Preprint. Discussion started: 21 January 2026

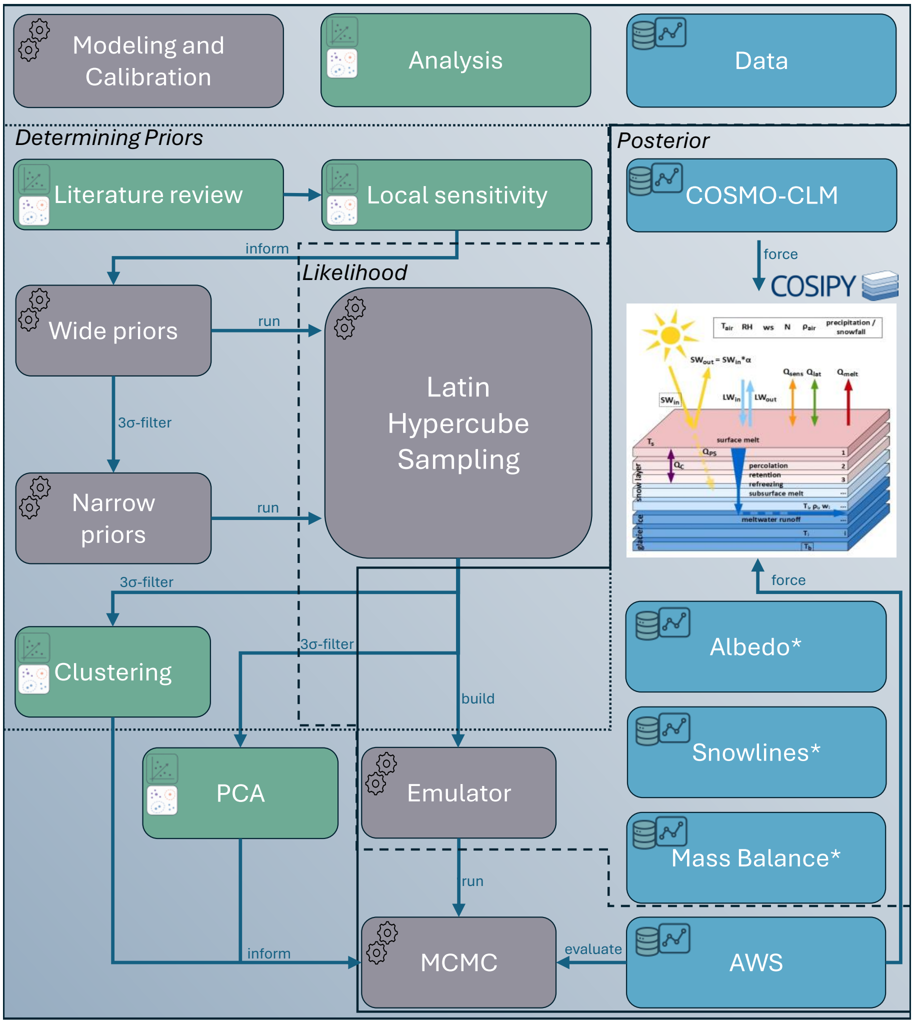

Figure 2. Overview of the workflow applied within this study. The dotted, dashed and solid lines highlight the respective elements used for the priors, the likelihood calculation and the posteriors. The observational datasets, highlighted with a star, of the glacier-mean albedo, snowlines and geodetic mass balances were used throughout the whole workflow as described in the text. To maintain overview, we have not drawn an arrow from the automatic weather station (AWS) to the Latin Hypercube Sampling nor from any other stage to the COSIPY model. We have roughly grouped the processes and tools into three categories, as outlined at the top of the figure, but these categories are not always clearly distinguishable. The COSIPY figure was adapted from Huintjes (2014).

2.4.1 Bayesian calibration framework

We used Bayesian inference (see, e.g., Gelman et al., 2013) to estimate the probability distribution of our model parameters θ and their associated uncertainties, neglecting explicit treatment of uncertainties in the forcing data or model physics. Following the approach from Rounce et al. (2020) and Sjursen et al. (2023, 2025), we assume that the calibration data represent the

https://doi.org/10.5194/egusphere-2025-6249
Preprint. Discussion started: 21 January 2026

truth, and that the output of the forward model (F; here COSIPY) deviates from this truth according to a normally distributed observational error and an unknown model error. Let $\boldsymbol{d}$ be the vector combining all N observations from our three observed data streams (B_{geod}, SLA and $\bar{\alpha}$). A single observation d_i is related to the model output y_i^{mod} by:

$$d_i = y_i^{\text{mod}} + \epsilon_i + \eta_i, \tag{11}$$

where $y_i^{\text{mod}} = F(\mathbf{X}, \theta)$ is the corresponding model output generated by one realisation of COSIPY produced by the climatological forcing data $\mathbf{X}$ with parameter choices θ. We define the Gaussian observational error ϵ_i with a mean of zero and a variance given by the respective observational product for each data point $\sigma^2_{\text{obs},i}$. The systematic error η_i accounts for any uncertainty not related to the parameter choices for example through missing processes or structural model errors. This error was set to zero during the accumulation season (here October to April) and we used it for the snowline and albedo data in the ablation season (May to September), since the model matches well the fully snow-covered winter conditions (not shown). We assume that both error terms are independent and η_i also has a mean of zero but an unknown variance $\sigma^2_{\eta,i}$ so that:

$$\epsilon_i \sim \mathcal{N}(0, \sigma^2_{\text{obs},i}) \tag{12}$$

$$\eta_i \sim \mathcal{N}(0, \sigma^2_{\eta,i}). \tag{13}$$

We estimate the standard deviation $\sigma_{\eta,i}$ as constant for all ablation season data points for SLA and $\bar{\alpha}$ with small magnitude half-normal priors chosen to be minimally invasive:

$$\sigma_\eta^{\text{SLA}} \sim \text{HalfNormal}(\sigma^2 = 0.03^2) \tag{14}$$

$$\sigma_\eta^{\bar{\alpha}} \sim \text{HalfNormal}(\sigma^2 = 0.02^2). \tag{15}$$

Combining the systematic model error and the observational error gives the total variance:

$$\sigma_i^2 = \sigma^2_{\text{obs},i} + \sigma^2_{\eta,i} \tag{16}$$

The foundation for the Bayesian inference is provided by Bayes' theorem (see, e.g., Gelman et al., 2013):

$$p(\theta|\boldsymbol{d}, \mathbf{X}) = \frac{p(\theta)p(\boldsymbol{d}|\theta, \mathbf{X})}{p(\boldsymbol{d})} \tag{17}$$

where $p(\theta)$ denotes the joint prior distribution of the parameters before any data is considered. The data vector $\boldsymbol{d}$ contains the observations B_{geod} (Hugonnet et al., 2021), SLA (Loibl, 2023; Loibl et al., 2025) and $\bar{\alpha}$ (Ren et al., 2021) as previously defined. The likelihood term $p(\boldsymbol{d}|\theta, \mathbf{X})$ is the probability distribution of the datasets given θ and $\mathbf{X}$ and $p(\boldsymbol{d})$ refers to the evidence or marginal distribution of the data (Gelman et al., 2013; Rounce et al., 2020). It acts as a normalising constant and is defined as:

$$p(\boldsymbol{d}) = \int p(\theta)p(\boldsymbol{d}|\theta)d\theta. \tag{18}$$

This integral is often intractable to calculate for complex model systems. Since it does not depend on θ, it is treated as a constant and the posterior can be reduced to:

$$p(\theta|\boldsymbol{d}, \mathbf{X}) \propto p(\theta) \cdot p(\boldsymbol{d}|\theta, \mathbf{X}), \tag{19}$$

https://doi.org/10.5194/egusphere-2025-6249
Preprint. Discussion started: 21 January 2026

assuming a given climate forcing $\mathbf{X}$ and no variations therein.

We assumed that the observations and their errors are independent. The joint likelihood function can then be simplified to:

$$p(\boldsymbol{d}|\theta,\mathbf{X}) = p(B_{\text{geod}}|\theta,\mathbf{X}) \cdot p(\text{SLA}|\theta,\mathbf{X}) \cdot p(\bar{\alpha}|\theta,\mathbf{X}) \tag{20}$$

which can be reduced to sums considering the log-likelihood. We defined the respective log-likelihood scores as the average over all data points for the mass balance (one point), SLA (58 points) and albedo values (98 points):

$$\mathcal{L} = \frac{1}{N}\sum_{i=1}^{N}\log\left[\frac{1}{\sqrt{2\pi}\sigma_i}\exp\left(-\frac{(y_i^{\text{mod}} - d_i)^2}{2\sigma_i^2}\right)\right]. \tag{21}$$

This log-likelihood score serves as direct input for the analysis of the model's parameter behaviour. To facilitate its interpretation, it can be viewed as a measure of quality of fit, with higher values indicating a better match between observations and simulations. To ensure the same weight when calculating the joint log-likelihood, we normalised each log-likelihood score (see Section S2).

2.4.2 Establishing priors and parameter behaviour

To reduce the number of tunable model parameters, we relied on a local sensitivity study based on previously published parameter ranges (more details in Section S1). After performing the one-at-a-time parameter perturbations, our final parameter selection includes all albedo-related parameters, as well as the roughness length of ice ($z0_{\text{ice}}$) and the precipitation scaling factor (p_{f}). These sensitivities are in line with previous sensitivity studies using the COSIPY model (Arndt et al., 2021; Temme et al., 2023; Khadka et al., 2024).

We performed a two-step Latin-Hypercube-Sampling, similar to Lecavalier and Tarasov (2025), to derive meaningful priors and provide a baseline for the development of the surrogate model and the investigation of the parameter behaviour. LHS ensures a random, stratified sampling behaviour by dividing each parameter's range into equally-sized probability density intervals. In the first iteration, we run 500 LHS samples with the literature-defined prior ranges for all parameters except α_{fs}, α_{firn} and α_{ice}, which we constrained using the Landsat-derived per pixel values (see Section 2.3 and Fig. S7 to S9). After filtering the data based on 3-σ residuals of the best performing simulation to the observed data, we run a second iteration of the LHS for 2500 samples with updated priors based on the filtered first iteration. The resultant 2500 parameter and output pairs provide the basis for the surrogate model. In the next step, we employed the same 3-σ filtering to retain 517 simulations. We refer to this as the COSMO-forced LHS ensemble. This ensemble was not used to actually run COSIPY but instead to provide a priori information on the model's parameter behaviour. A detailed description of both approaches is provided in the Supplementary material, and an overview of the applied parameters and their ranges can be found in Table 1.

To identify which parameter combinations can produce similar model results (i.e., equifinality), we employed a Spearman rank correlation on the COSMO-forced LHS ensemble. This method cannot capture non-monotonic relationships, and we therefore correlated parameters against each other and against the model bias for each of the three observational datasets. This serves as a first-order approximation of parameter interactions only, as the model system is highly non-linear (e.g., Johnson and Rupper,

https://doi.org/10.5194/egusphere-2025-6249
Preprint. Discussion started: 21 January 2026

2020). These methods were supported by a Principal Component Analysis (PCA) based on the standardised parameter vectors of the COSMO-forced LHS ensemble.

To understand which datasets constrain specific parameters, we applied K-Means clustering to the 517 ensemble members. We grouped the simulations into four clusters based on the joint log-likelihood scores and the individual log-likelihood scores for each observed dataset, respectively. These clusters were investigated to identify differences in parameter distributions and isolate the effect of the observed data on each parameter value. The parameter distributions of the best-performing cluster were transformed into truncated normal distributions, serving as the priors for the MCMC. An overview of the main methodology is provided in Figure 2.

Table 1. Table of the prior parameter with two-floating point precision. The literature-derived parameter ranges served as the uniform input for the local sensitivity study, the values of the first LHS stage (LHS1) as uniform priors to the LHS1 and so forth. The prior ranges for the MCMC are truncated normal distributions and were derived from the best-performing LHS2 cluster (see Section 2.4.2). Parameters highlighted in bold were deemed sensitive and used for the calibration.

Parameter	Unit	Literature Range	LHS1	LHS2	MCMC (μ, σ, lower, upper)
Albedo of fresh snow (α_{fs})	-	0.75 to 0.98	0.89 to 0.93	0.89 to 0.93	$\mathcal{N}_{\mathrm{T}}$(0.90, 0.1, 0.89 - 0.93)
Albedo of ice (α_{ice})	-	0.10 to 0.46	0.12 to 0.23	0.12 to 0.23	$\mathcal{N}_{\mathrm{T}}$(0.18, 0.1, 0.12, 0.23)
Albedo of firn (α_{firn})	-	0.46 to 0.75	0.51 to 0.69	0.51 to 0.69	$\mathcal{N}_{\mathrm{T}}$(0.60, 0.1, 0.52, 0.68)
Albedo aging factor (α_{aging})	days	1.0 to 25.0	1.0 to 25.0	2.0 to 25.0	$\mathcal{N}_{\mathrm{T}}$(13.82, 5.37, 5.07, 24.77)
Albedo depth scale (α_{depth})	cm	1.0 to 15.0	1.0 to 15.0	1.0 to 14.2	$\mathcal{N}_{\mathrm{T}}$(1.78, 0.67, 1.0, 4.0)
Roughness length of fresh snow ($z0_{\mathrm{fs}}$)	mm	0.02 to 1.6	-	-	-
Roughness length of ice ($z0_{\mathrm{ice}}$)	mm	0.7 to 20	0.7 to 20	0.7 to 20	$\mathcal{N}_{\mathrm{T}}$(8.61, 9, 1.2, 19.65)
Roughness length of firn ($z0_{\mathrm{firn}}$)	mm	1.6 to 6.5	-	-	-
Aging factor roughness ($z0_{\mathrm{aging}}$)	$\mathrm{mm\,h^{-1}}$	0.0013 to 0.0039	-	-	-
Precipitation factor (p_{f})	-	0.5 to 2.0	0.5 to 2.0	0.57 to 1.342	$\mathcal{N}_{\mathrm{T}}$(0.78, 0.08, 0.65, 0.95)

2.4.3 Calibration with MCMC and surrogate model for COSIPY

To robustly quantify parameter uncertainty in the COSIPY model, we ran an MCMC calibration which generates samples from the otherwise analytically challenging joint posterior distribution. The calibration procedure involved 15 independent MCMC chains, each run for 100,000 samples following a 10,000-sample burn-in phase using the Metropolis-Hastings algorithm implemented with the open source PyMC (Abril-Pla et al., 2023). The chains were initialised at 15 dispersed starting points drawn from a Latin Hypercube Sample to ensure a thorough exploration of the parameter space. Based on the result of the parameter inference and identifiability provided in Section 3.1, we performed a two-step calibration first using $\bar{\alpha}$ and B_{geod} as calibration targets and then using SLA similar to the setup employed in Aschwanden and Brinkerhoff (2022).

While we did not explicitly test for the minimum required chain length and burn-in phase, initial testing revealed that the problem's complexity and the resulting strong autocorrelation rendered shorter chains on the order of 10^4 to $2 \cdot 10^4$ and smaller

https://doi.org/10.5194/egusphere-2025-6249
Preprint. Discussion started: 21 January 2026

burn-in phases (e.g., 2000 samples) insufficient for achieving robust convergence. We evaluated chain convergence and posterior parameter distributions using all available samples. To evaluate the model performance in comparison to the various observations, we created a posterior ensemble. To do so, we reduced the $15 \cdot 10^5$ samples by first thinning the posterior series based on the results of the convergence diagnostics (see Section 3.2.1) and then taking 300 random samples to re-run the full COSIPY model.

We circumvented the high computational cost of running the full COSIPY model for thousands of parameter sets by using the output of the second LHS stage to develop three surrogate models replicating the required COSIPY output. The 2500 LHS simulations were partitioned into a training set of 2000 and a validation set of 500 samples. The surrogate is built as a three-branch neural network, taking an input vector of the standardised COSIPY parameters and a temporal encoding of the snowline and albedo observing time, and predicting the mean annual mass change rate for 2000 to 2010, the SLA, and $\bar{\alpha}$ at the same time. The mass balance branch consists of a simple multilayer perceptron (Rumelhart et al., 1986) with two dense hidden layers, while the snowline and albedo branch relies on a recurrent neural network built around bidirectional long short-term memory layers (Hochreiter and Schmidhuber, 1997; Schuster and Paliwal, 1997). Since the forcing data, except for the precipitation field, stays constant between samples, we do not include time-lagged forcing fields, relying on the neural network to learn their effect as a stationary background forcing implicitly. The surrogates show a good performance when compared to the independent test data, and we deem them an acceptable substitute for COSIPY (see Fig. S10 to S12).

2.4.4 Model evaluation with in-situ data

We evaluated the performance of the calibrated model by conducting posterior predictive checks using the 300-member ensemble drawn from the thinned posterior distribution. In addition, the calibrated model performance was compared to the mass balance profiles reported by the WGMS (2024), to the geodetic results of Klug et al. (2018), the on-glacier AWS data and to a COSIPY model ensemble partially forced and calibrated with the AWS data.

Two AWS were installed at HEF in the hydrological year 2003/04, one at the tongue at 2640 m a.s.l. and one in the accumulation area at 3048 m a.s.l. These stations recorded air temperature and humidity at 2.5 m, wind speed and wind direction, all radiation components, surface height change and snow temperature (Olefs and Obleitner, 2007; Obleitner, 2022) although the true measurement height varied substantially between 0.5 m and 2.7 m (Schrott, 2006). As the lower station suffered from numerous system failures and data gaps, we focus our evaluation on the upper station, using the lower station as a qualitative reference only. Although the data provided at hourly resolution (Obleitner, 2022) come in a clean format, we performed several quality checks and corrections. For the sake of brevity, we refer the reader to Nicholson et al. (2013) for an overview of the correction methods. We only deviated in the calculation of saturation vapour pressure by using the equation provided by Huang et al. (2018). Atmospheric pressure for the 2003/04 hydrological year was extrapolated from a station at Pitztaler Glacier (GeoSphere Austria, 2024) for both stations.

The upper station data was used as in-situ forcing for COSIPY in order to examine how the energy flux partitioning differs between model simulations calibrated with remotely sensed data and in situ data. Since the AWS did not record total precipitation, we instead inserted the COSMO-simulated field, thereby minimising differences caused by the precipitation time series

https://doi.org/10.5194/egusphere-2025-6249
Preprint. Discussion started: 21 January 2026

but creating a not entirely measured benchmark. We did not provide the model with the measured time series of α and Q_{LWout}, instead focusing on achieving the best possible model performance given better-resolved meteorological forcing fields and calibration data. Thus, we force an assessment of physical coherence and parameterisation performance, but must acknowledge that this reference does not necessarily correspond to the physical truth.

COSIPY was initialised at the start of October 2002 with a snow height of zero and all other initial conditions taken from the COSMO-forced simulations. We repeated the forcing data for the hydrological year 2003/04 to allow for model spin-up and ran 7500 LHS iterations. The 7500 simulations were then filtered based on a ten percent deviation from the best solution according to the sum of normalised Root Mean Squared Errors (RMSE) computed with measured daily surface height change, Q_{LWout} and albedo. The final ensemble consists of 67 members and we henceforth refer to it as the AWS-assisted ensemble. The SEB conditions were then evaluated using five-day rolling means.

3 Results

This section first analyses the parameter identifiability, that is, the possibility of uniquely determining model parameters from the data, and their compensating effects based on the COSMO-forced LHS ensemble and the correlation and PCA analysis. Next, we assess the parameter inference from the different data streams by determining which observations influence which parameter selection using the K-means clustering. Afterwards, the performance and posterior distributions of the parameter calibration using the MCMC are investigated and assessed in comparison to existing literature and various in-situ observations, including glacier-wide mass balances and AWS measurements. Lastly, the SEB is evaluated in comparison to the AWS-assisted ensemble as detailed in Section 2.4.4.

3.1 Parameter inference and identifiability

The correlation heatmap (Fig. 3) shows the correlation strength between model parameters and the simulation biases of the COSMO-forced LHS ensemble. We find that p_{f} exerts a strong influence on the model system, with large absolute correlations ($|\rho| > 0.4$) across all three biases. That said, the strongest parameter and model output correlation (ρ = 0.73) is between α_{aging} and the albedo bias $\Delta\bar{\alpha}$. $\Delta\bar{\alpha}$ also shows a smaller but significant correlation to α_{fs} and α_{firn}. This correlation would likely be greater if the α_{fs} range were left unconstrained.

We attribute the absence of similar distinct signals for snowline and mass balance biases and the weaker correlation of the other parameters ($|\rho|$ < 0.25) to the limitations of the Spearman rank correlation as it only captures monotonic correlations between single parameters. This correlation absence is even more pronounced under persistently snow-covered conditions that can completely suppress the sensitivity of parameters such as α_{ice} (see Fig. S4). Thus, the model output variability induced by p_{f} suppresses the influence of other parameters. We also find that biases of mass balance, snowlines, and albedo are strongly correlated, in contrast to the assumptions we made during the definition of our Bayesian framework. A negative correlation between p_{f} and α_{aging} (ρ = -0.64) highlights the primary mode of parameter compensation in COSIPY, confirmed by the PCA analysis, which also indicates a parameter space with strong potential for equifinality (Fig. S14).

https://doi.org/10.5194/egusphere-2025-6249
Preprint. Discussion started: 21 January 2026

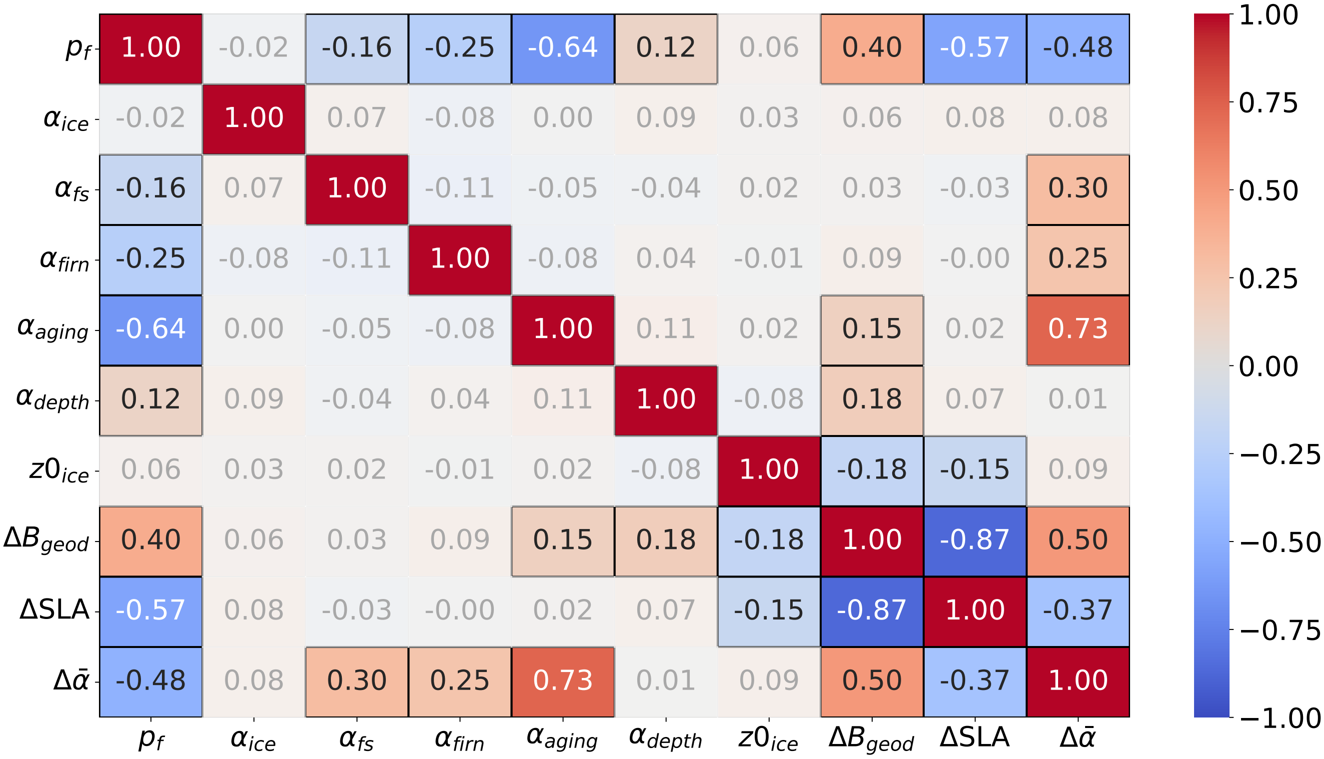

Figure 3. Spearman rank correlation heatmap of the COSMO-forced Latin Hypercube Sample ensemble (n=517). Only statistically significant correlations are displayed in colour ($p < 0.01$). The parameters are defined as summarised in Table 1, while ΔB_{geod}, ΔSLA, $\Delta\bar{\alpha}$ refer to the biases between simulated and observed values.

The K-means cluster analysis (Fig 4) based on the joint log-likelihood score reveals a single high-performing group of parameter sets (Cluster 4) but also tension between the observational constraints. The best-performing Cluster 4 is characterised by a high joint log-likelihood score (median = 2.27) driven by strong fits to both SLA (median = 1.30) and $\bar{\alpha}$ (median = 1.01). This cluster does not produce the optimal fit for B_{geod}, which instead shows the largest log-likelihoods in Cluster 1. This illustrates the difficulty of satisfying all three observational constraints simultaneously. For example, the best-performing cluster for the SLA shows a large spread in log-likelihood (and thus performance) for the other log-likelihood scores. Conversely, clusters that perform best for B_{geod} or $\bar{\alpha}$ show worse scores for the SLA log-likelihood (red and blue distributions in panel j). The analysis of Cluster 4 reveals strong constraints on p_{f} with an interquartile range (IQR) of 0.73 to 0.83, α_{fs} (IQR: 0.89 to 0.91), α_{aging} (IQR: 9.30 to 17.28 days) and α_{depth} (IQR: 1.28 to 2.05 cm). While $\bar{\alpha}$ provides the tightest constraints on albedo-specific parameters (α_{fs} and α_{aging}), the SLA observations primarily determine α_{depth} and compared to the other scores prefers a lower p_{f}. The other parameters, including α_{ice}, α_{firn} and $z0_{\text{ice}}$, are only marginally constrained by the B_{geod} and $\bar{\alpha}$. This signal is largely obscured in the joint log-likelihood because of their comparably low sensitivity, and a denser sampling of the parameter space might better resolve their optimal range.

https://doi.org/10.5194/egusphere-2025-6249
Preprint. Discussion started: 21 January 2026

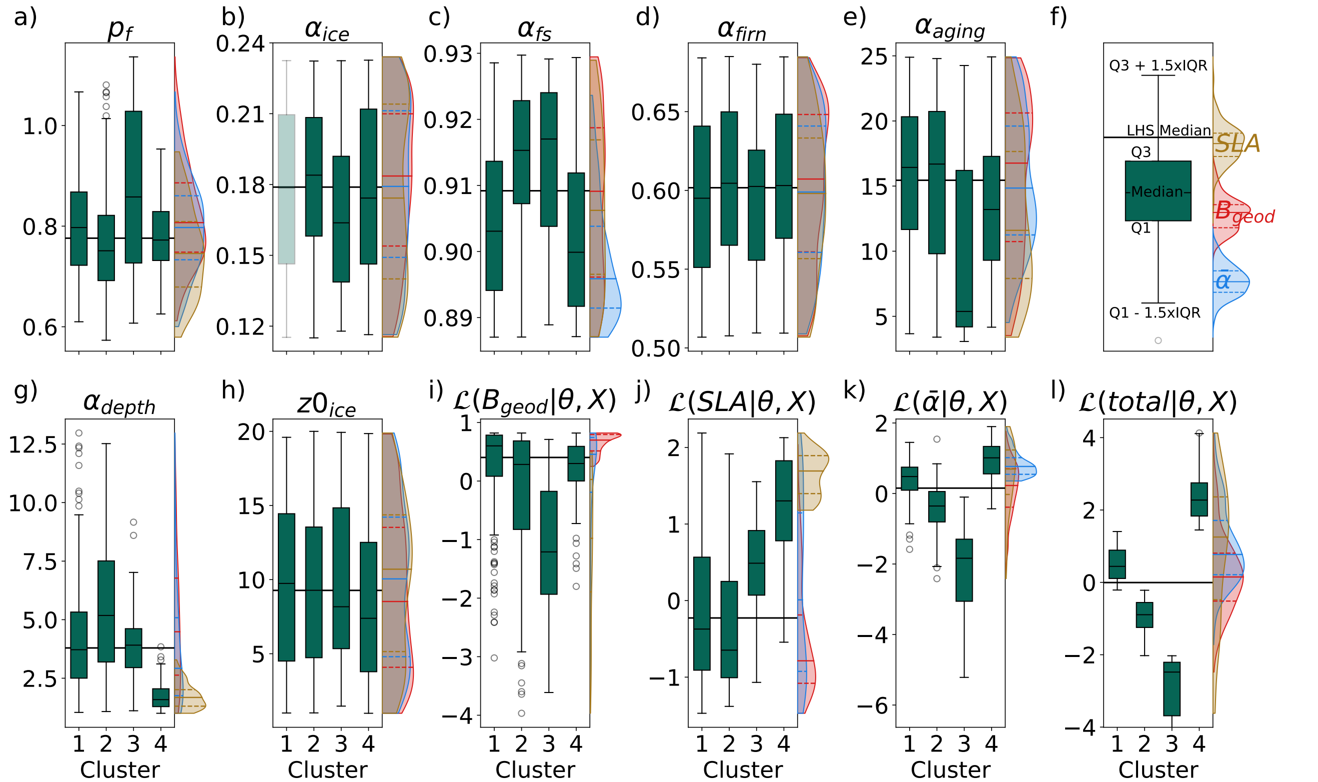

Figure 4. Boxplots of parameter values based on the K-means clustering of the COSMO-forced Latin Hypercube Sampling ensemble in panels a) to e) and g) to h). Panel f) displays the subplot legend, while panels i) to l) show the log-likelihood scores for B_{geod}, SLA, $\bar{\alpha}$ and their sum $\mathcal{L}(total|\theta, \mathbf{X})$. The side panels display the parameter distributions of the best-performing cluster, clustering based on only snowline altitudes (yellow), mass balances (red), and albedo (blue) as defined in text. The horizontal line denotes the median of the COSMO-forced Latin Hypercube Sampling ensemble (n=517).

3.2 Calibration results

3.2.1 Convergence diagnostics

Visual inspection of the trace plots for the log-likelihood (Fig. 5) and all individual parameters (Fig. A1) show stable, well-mixed, and converging chains. This is confirmed by several convergence diagnostics, including the Gelman-Rubin statistics $\hat{R}$, the effective sample size (ESS), the integrated autocorrelation time (IAT), and the Monte Carlo standard error (MCSE). The $\hat{R}$ is approximately 1.0 for all parameters, indicating that all chains converged to the same target distribution. The ESS ranges from 32,000 to 85,000 for both bulk and tail estimates, demonstrating a very high number of independent samples. Furthermore, numerical uncertainty in the posterior is negligible, with MCSE values for the posterior mean and standard deviation well

https://doi.org/10.5194/egusphere-2025-6249
Preprint. Discussion started: 21 January 2026

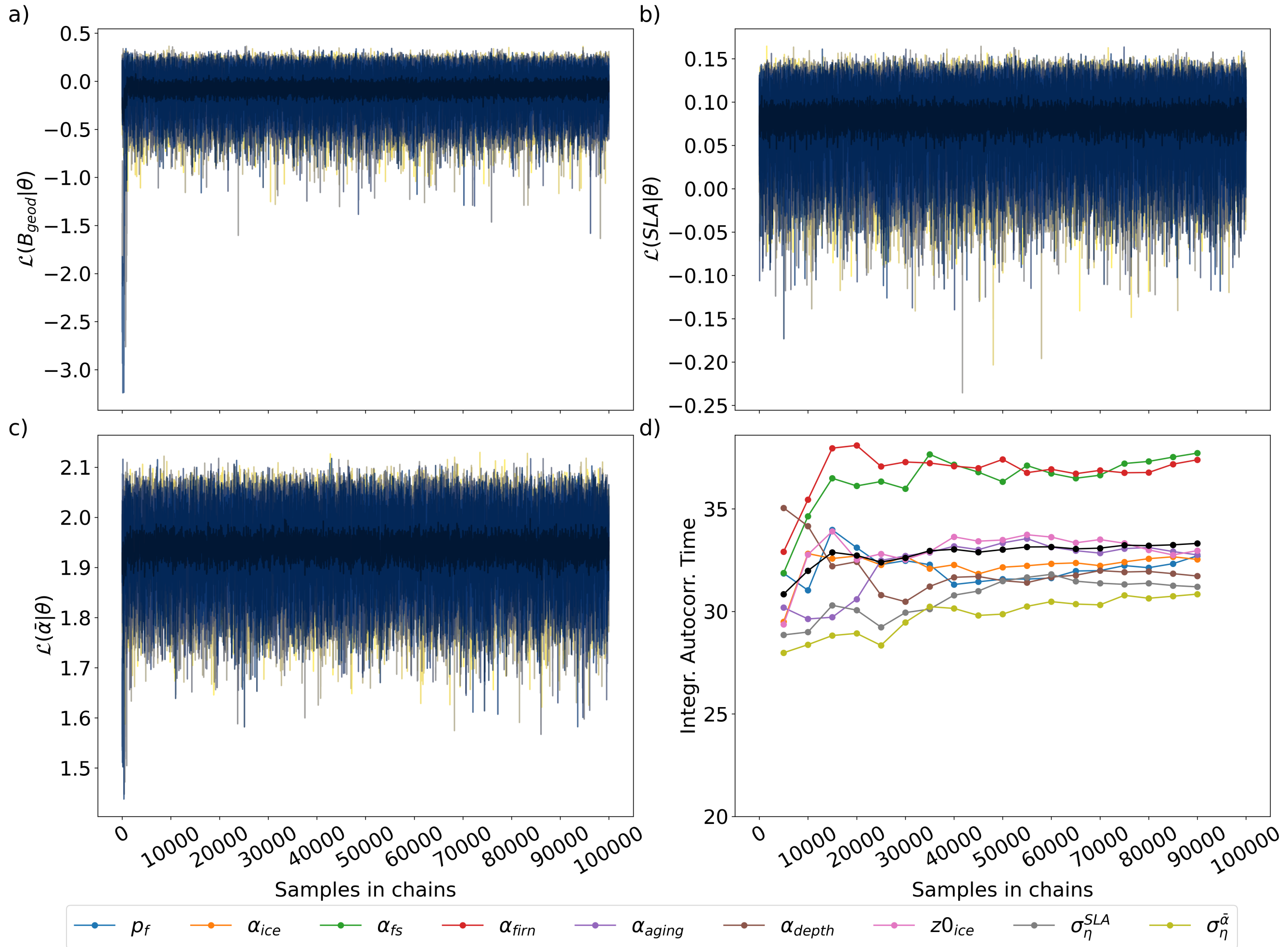

Figure 5. Traces of the fifteen chains and the 100,000 posterior samples of the log-likelihood for mass balance, snowlines and mean glacier albedo (a to c). The mean across chains is displayed in black. Panel d) shows the integrated autocorrelation time per parameter, averaged across the chains. The black line in panel d) corresponds to the mean integrated autocorrelation time of all parameters.

below 0.15% and 0.1% of the 95% credible interval (CI) width, respectively. The IAT stabilise at values between 25 and 40. Therefore, we thinned the posterior distributions by retaining every 40th sample for the model evaluation (see Section 2.4.3).

3.2.2 Posterior parameter distributions

Comparing prior and posterior parameter distributions, we find that the data provide strong constraints on all model parameters, significantly narrowing their distribution compared to the LHS-based priors (Fig. A1). The posterior for α_{depth} is strongly constrained with a mean of 1.01 cm and a 95% CI of 0.99 to 1.03 cm. For brevity, we report this and subsequent results as the posterior mean, followed by the 95% credible interval in brackets.

https://doi.org/10.5194/egusphere-2025-6249
Preprint. Discussion started: 21 January 2026

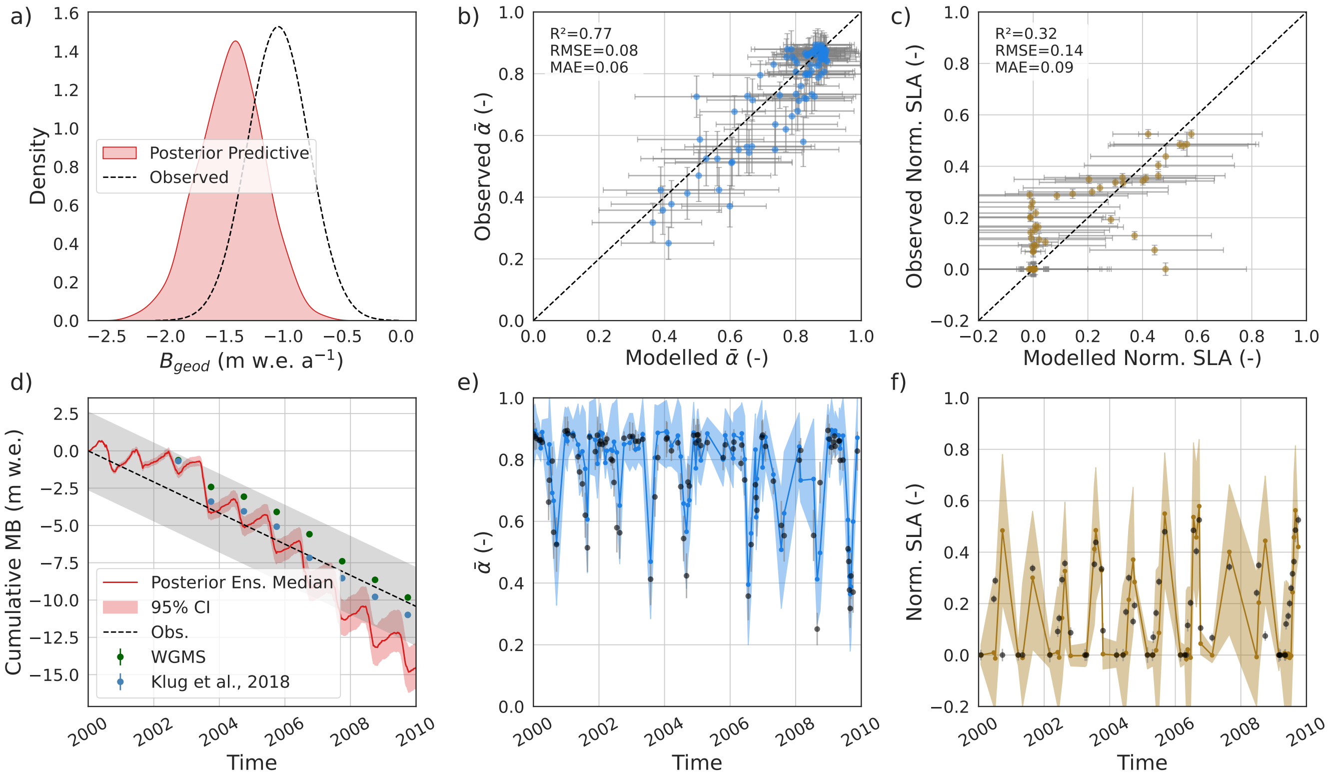

Figure 6. Posterior predictive checks for mass balance in red (left), albedo in blue (centre) and snowlines in yellow (right). Green and blue dots in panel d) show observed annual mass balances, and dots in panels e) and f) correspond to the observed data points. Points in the time series were interpolated between observed times and do not necessarily reflect the model state at those times. The shading combines the parametric 95% credible interval and the systematic errors. Note that the cumulative mass balance comparison (d) does not show a posterior predictive check.

The posterior probability of the albedo parameters α_{ice}, α_{firn} and α_{fs} are well defined around values of 0.23 [0.22, 0.24], 0.64 [0.62, 0.67] and 0.89 [0.88, 0.90], respectively. Consistent with the inference strength identified previously, both p_{f} and α_{aging} are strongly constrained to ranges of 0.70 [0.69, 0.73] and 14.21 [12.46, 15.95] days, respectively, despite their compensating effects. The posterior pair plots confirm that compensating effects are largest between α_{firn}, α_{aging}, and p_{f} (Fig. S15). The least constrained parameter is $z0_{\mathrm{ice}}$, with 3.16 [0.7, 5.63] mm, confirming its weaker inference signal from the clustering analysis. Lastly, both systematic ablation season error terms ($\sigma_{\eta}^{\mathrm{SLA}}$ and $\sigma_{\eta}^{\bar{\alpha}}$) are identified at the tails of their prior distributions. This indicates a strong inference signal from the data, allowing the model to quantify the magnitude of its structural uncertainty. While $\sigma_{\eta}^{\bar{\alpha}}$ is relatively small and comparable to the observational uncertainty (0.06 [0.04, 0.07]), $\sigma_{\eta}^{\mathrm{SLA}}$ is substantially larger (0.14 [0.12, 0.16]). The strong constraint on both error terms confirms a systematic model limitation that is successfully captured by the error model. These results are stable across all chains.

https://doi.org/10.5194/egusphere-2025-6249
Preprint. Discussion started: 21 January 2026

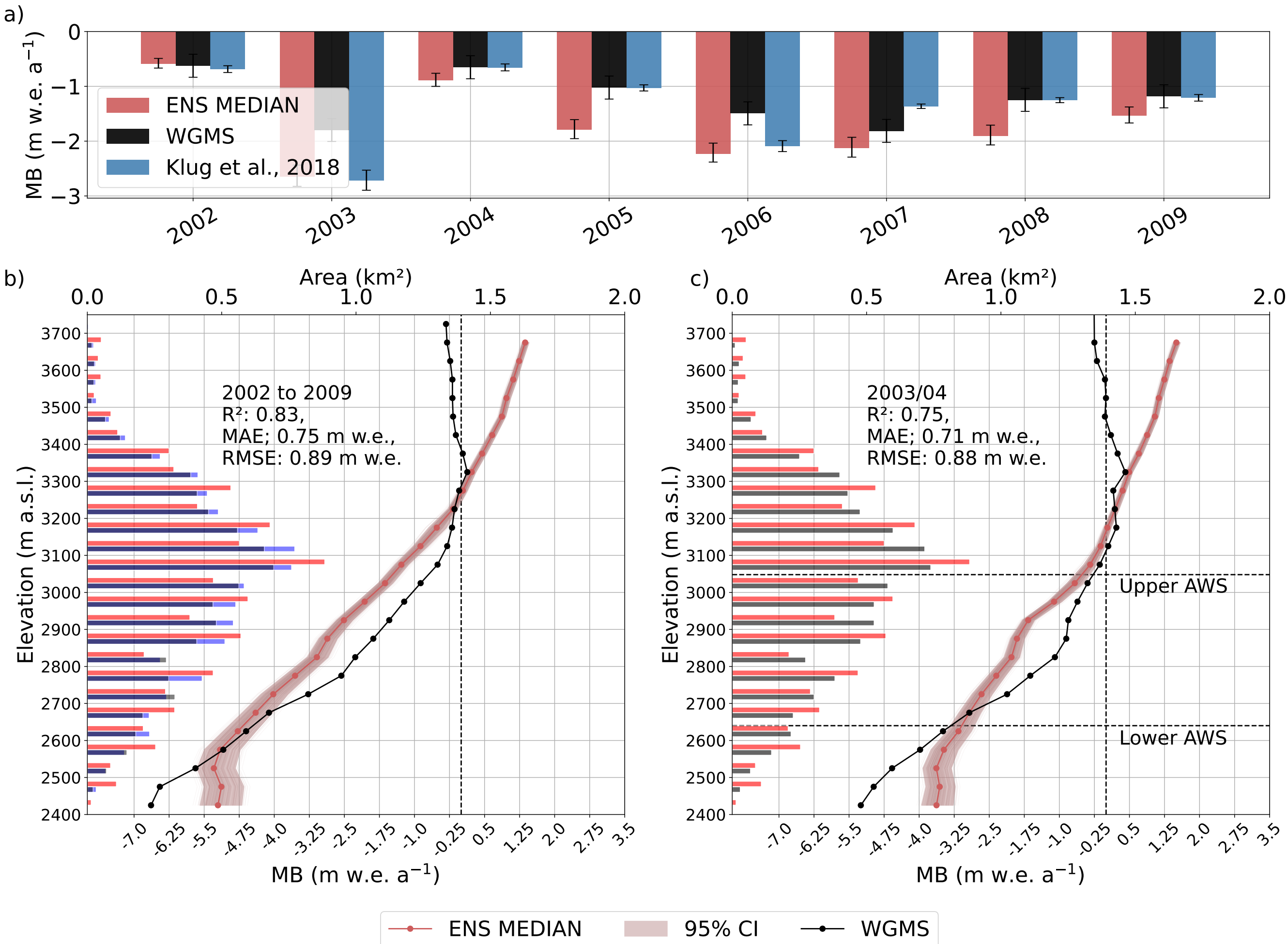

Figure 7. Panel a) shows the comparison of modelled glacier-wide mean annual mass balances as recorded by WGMS (2024) and Klug et al. (2018) and this study's posterior ensemble median and the respective uncertainties for the hydrological years 2002 to 2009. Uncertainties in the COSIPY ensemble refer to the 95% credible interval. The bottom panels show the average hypsometry and mass balance gradients for the same years (b) and just those for the hydrological year 2004, where AWS measurements were available (c). The glacier area is related to the top x-axis and shown in red for COSIPY (constant in time), and for 2002 (blue) and 2009 (grey) in the left subplot and for the hydrological year 2004 as derived from the WGMS in the right subplot in grey. The bottom x-axis shows the mean annual mass balance per 50 m elevation band, as recorded in WGMS (2024). The simulated 20 m elevation bins are aggregated to 50 m elevation bins using an area-weighted average. Note that these bands do not perfectly add up.

https://doi.org/10.5194/egusphere-2025-6249
Preprint. Discussion started: 21 January 2026

3.3 Calibrated model performance and validation

3.3.1 Posterior Predictive Checks

The posterior predictive checks are displayed in Figure 6, representing the posterior ensemble output alongside the observational data from all three datasets. The shaded envelopes represent the 95% CI, reflecting both parameter uncertainty and the calibrated systematic error terms. The posterior predictive checks reveal a negative bias of B_{geod} with a simulated mean at -1.44 m w.e.a^{-1} compared to the observed -1.04 m w.e.a^{-1} (Hugonnet et al., 2021). Nevertheless, there is no significant statistical difference between both distributions, as indicated by a Kolmogorov-Smirnov test ($p > 0.05$). The mass balance bias is also apparent in the diverging simulated cumulative mass balance in comparison to B_{geod} (panel d in Fig. 6) of both geodetic estimates (Klug et al., 2018; Hugonnet et al., 2021) and the end-of-year glaciological mass balance (WGMS, 2024). This bias can be effectively eliminated by increasing p_{f}, which produces a good match with both WGMS and geodetic observations. We revisit this important point in the discussion section.

In contrast, the posterior ensemble median demonstrates a strong fit to $\bar{\alpha}$, with an R^2 of 0.77 and an RMSE of 0.08 with respect to the observations. The time series (panel e in Fig. 6) shows the extended 95% CI bracketing nearly all observational points and a general well-replicated progression of $\bar{\alpha}$. However, this strong performance must be qualified. First, the dataset mainly contains snow-covered scenes, which also affects the SLAs. This actually makes the calibration task easier. Second, achieving this fit still requires a systematic error term for ablation season albedo values, whose mean of 0.06 is nearly as large as the RMSE. The model successfully matches the overall progression of the mean glacier-wide albedo from its winter maximum (~ 0.9) to its summer minimum (~ 0.26). Nevertheless, the model often fails to capture the lowest summer albedo values, showing a positive bias when the glacier is not fully snow-covered.

The fit to the normalised SLA is considerably weaker (R^2 = 0.30, RMSE = 0.14) and reveals a structural deficiency, which is confirmed by the large systematic error estimated during calibration. A comparison of modelled and observed snowlines reveals two error features. The first feature is an overestimation of the SLA. The smaller overestimations occur primarily during times of observed maximum SLA, while larger ones are found during the ablation season when summer snowfall might have occurred (e.g., Voordendag et al., 2023).

The second feature is a negative bias, where the model simulates a snow-covered glacier while observations show exposed glacier ice. This occurs more often than the positive biases and indicates a systematic delay in the simulated snow melt-out date.

3.3.2 Mass balances

The mismatch between the posterior ensemble median and observed mass balance gradients points to a limitation in the representation of physical processes or forcing data (Fig. 7). Most notably, the model ensemble overestimates the mass balance at high elevations compared to the glaciological method in the hydrological years 2002 to 2009. While the ensemble shows steadily increasing mass balances with elevation up to 1.37 m w.e.a^{-1} at elevations above 3625 m a.s.l., the glaciological mass balance has its most positive value at ~3325 m a.s.l. and reaches negative mass balances up to -0.30 m w.e.a^{-1} at higher

https://doi.org/10.5194/egusphere-2025-6249
Preprint. Discussion started: 21 January 2026

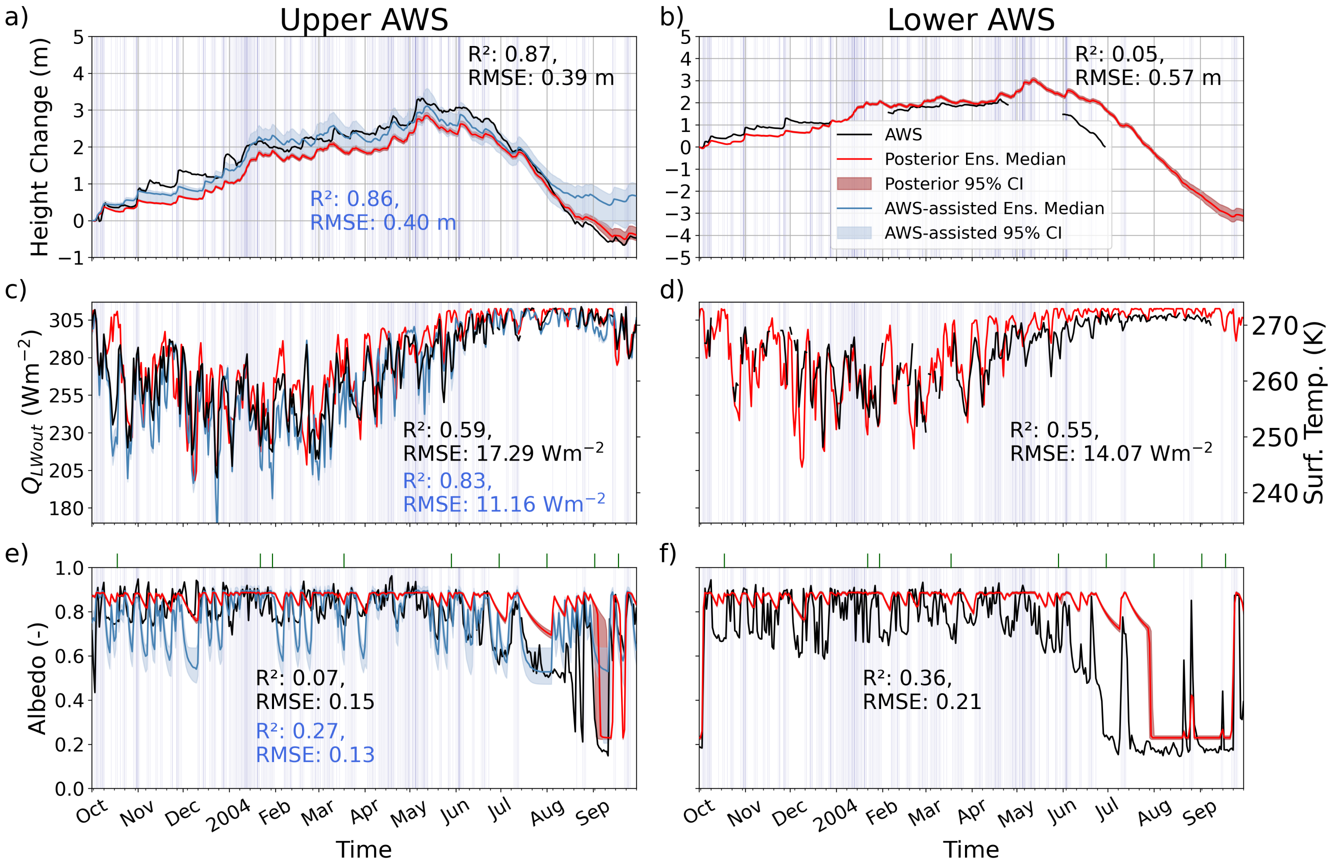

Figure 8. Comparison of daily means of measured surface height change (a, b), outgoing longwave radiation (c, d) and albedo (e, f) at the upper (left) and lower (right) AWS stations. The red line and shading show the posterior ensemble median and 95% credible interval, while the blue line and shading refer to the weighted median and 95% credible interval derived from the AWS-assisted ensemble. The black line shows the AWS measurements and metrics refer to the posterior ensemble median (black) or the AWS-assisted weighted median (blue). Background stripes indicate days with snowfall in the COSMO forcing.

elevations. Similarly, mass balances are less negative than observations at lower elevations by up to 1.43 m w.e.a^{-1}. At the glacier scale, these biases are cancelled out by simulating consistently more negative mass balance than observations (mean bias of -0.69 m w.e.a^{-1}) between 2625 m a.s.l. and 3175 m a.s.l., where the majority of the glacier area resides. Consequently, the annual glacier-wide mass balances show a negative bias compared to the WGMS data (Table 2 and Fig. 7a)).

On an annual basis, we find that the model aligns more closely with the geodetic results of Klug et al. (2018) in most years, except for the hydrological years 2004/05 and 2006/07. This is reflected in the mean absolute errors (MAE) of 0.38 and 0.50 m w.e.a^{-1} to the geodetic observations of Klug et al. (2018) and the WGMS. The WGMS reference series has known limitations related to the point data extrapolation in the years 2002/03, 2005/06, and 2006/07, when the absence of glaciological data above 3000 m a.s.l. led to significant mass balance overestimations (2002/03 and 2005/06) and an underestimation in

Table 2. Comparison of modelled and observed glacier-wide mass balance between the posterior ensemble with constant glacier area, and the homogenised records of Klug et al. (2018) and the WGMS (2024). All displayed values are reported in m w.e. and σ refers to the related random uncertainties as outlined in Klug et al. (2018), while we report the credible interval (CI) for the posterior ensemble.

Hydrological Year	Modelled (COSIPY)		Observed (WGMS)		Observed (Klug et al., 2018)	
	MB	95% CI	MB	σ	MB	σ
2001/02	-0.587	[-0.667, -0.49]	-0.624	0.21	-0.685	0.062
2002/03	-2.647	[-2.824, -2.437]	-1.796	0.21	-2.713	0.183
2003/04	-0.892	[-1.002, -0.761]	-0.651	0.21	-0.654	0.063
2004/05	-1.791	[-1.954, -1.607]	-1.022	0.21	-1.028	0.056
2005/06	-2.228	[-2.382, -2.036]	-1.493	0.21	-2.091	0.1
2006/07	-2.129	[-2.292, -1.930]	-1.813	0.21	-1.363	0.041
2007/08	-1.905	[-2.069, -1.708]	-1.246	0.21	-1.252	0.046
2008/09	-1.536	[-1.669, -1.376]	-1.182	0.21	-1.209	0.06

2006/07 (Klug et al., 2018). We find that COSIPY adequately captures the extremely negative mass balances in 2002/03 associated with the European heatwave (e.g., Schär et al., 2004; Huss et al., 2008; Braithwaite et al., 2013). Generally, COSIPY reproduces the observed interannual mass balance variability well, as evidenced by high correlation coefficients of r = 0.87 and r = 0.93 with Klug et al. (2018) and the WGMS observations, respectively.

3.3.3 Surface Energy Balance conditions

Net shortwave radiation (Q_{SWnet}) is the largest energy source throughout the year, similar to other mid-latitude glaciers (Cuffey and Paterson, 2010; Chen et al., 2023). Unless stated otherwise, we report all energy balance terms as five-day rolling means. The posterior ensemble's five-day rolling means range from 2 to 40 $\mathrm{W m^{-2}}$ in the accumulation season to 16 to 176 $\mathrm{W m^{-2}}$ in the ablation season (panel a in Fig. 9). The posterior ensemble shows little variability in the SEB components associated with the high confidence in the posterior parameters and prevailing snow cover until July 2004. Uncertainty increases significantly in September when different parameter combinations produce varied snow melt-out dates (Fig. 8e)). When Q_{SWnet} peaks at 176 $\mathrm{W m^{-2}}$ in September, the available melt energy Q_{ME} also peaks at -147 $\mathrm{W m^{-2}}$, indicating substantial surface melting (see also Fig. 8a)).

This energy source is mildly moderated by the net longwave radiation (Q_{LWnet}). The good fit to the observed Q_{LWout} confirms a systematic overestimation of the Q_{LWin} in the posterior ensemble (see also Fig. A2d). Thus, Q_{LWnet} acts only as a small energy sink throughout the year (mean -15.36 $\mathrm{W m^{-2}}$), except in early August when it reaches 20.66 $\mathrm{W m^{-2}}$.

Q_{H} is an energy source, except from May to June when the surface is warmer than the air. During winter, Q_{H} can amount to 30 $\mathrm{W m^{-2}}$ (Fig. 8c) and the flux peaks at 49 $\mathrm{W m^{-2}}$ in early September. Q_{E} reaches 37 $\mathrm{W m^{-2}}$ between June and August when

https://doi.org/10.5194/egusphere-2025-6249
Preprint. Discussion started: 21 January 2026

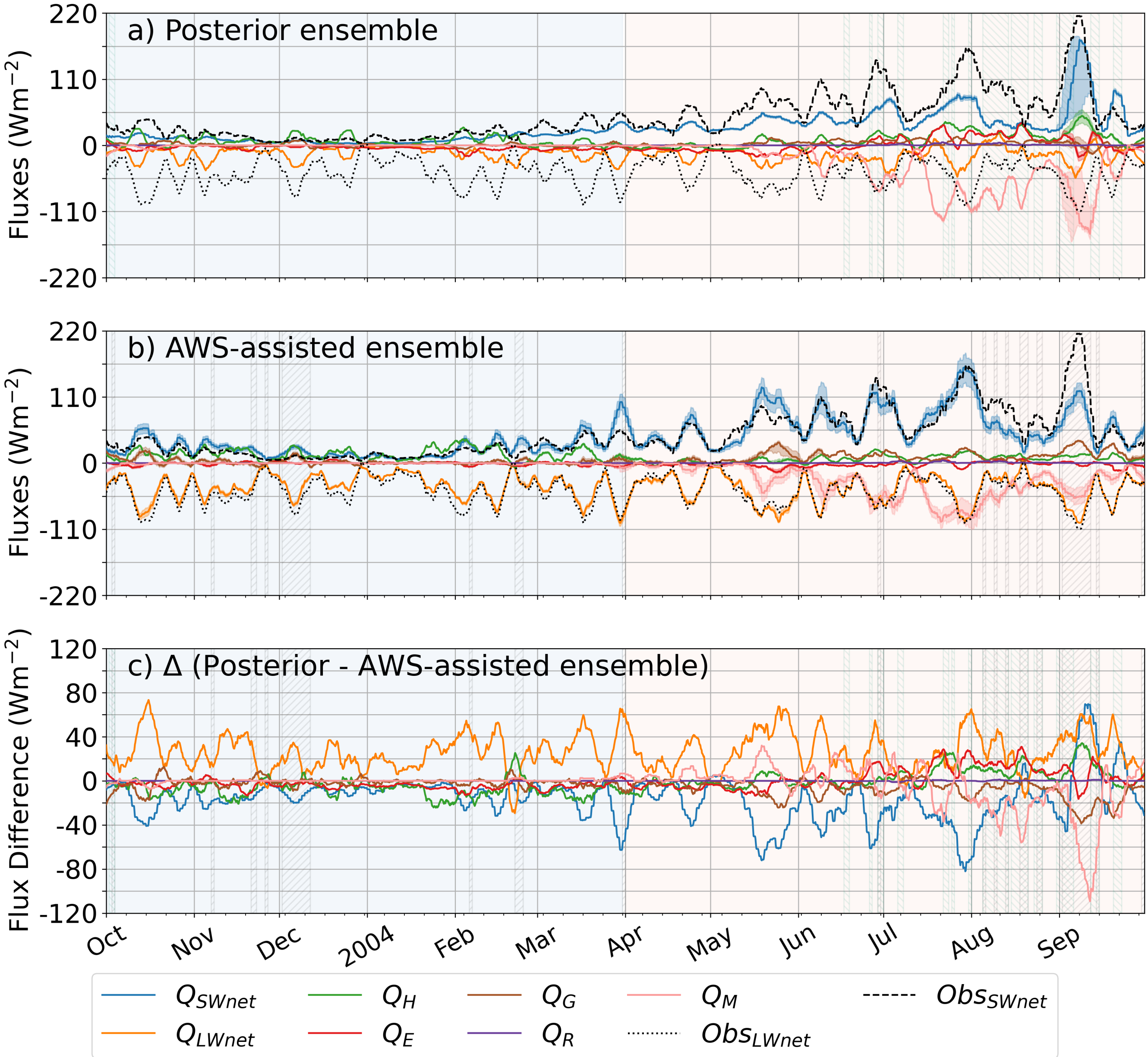

Figure 9. Five-day rolling means of the surface energy balance fluxes as simulated by the posterior ensemble median and 95% credible interval (a) and the AWS-assisted ensemble and its weighted median and 95% credible interval (b). Panel c) shows the flux difference between the two. Fluxes are defined as in text and the black dotted and dashed line show AWS-observed Q_{LWnet} and Q_{SWnet}, respectively. The hatchings indicate days where the mean absolute error between simulated and observed albedo is larger than 0.2, and accumulation season (light blue) and ablation season (light orange) are separated by background shading.

https://doi.org/10.5194/egusphere-2025-6249
Preprint. Discussion started: 21 January 2026

condensation is largest (Fig. S22). This partly coincides with the positive Q_{LWnet} contribution, suggesting high air moisture and cloud cover which may indicate frequent convection and thunderstorms. Both fluxes are however also linked through their parameterisation based on air temperature and humidity. For the rest of the year, Q_{E} fluxes are near zero or a small energy sink as evidenced by the year-round sublimation (Fig. S23). Q_{R} is negligible throughout the year. Similarly, Q_{G} provides only a small positive contribution in summer with an annual amplitude of -14 to 14 $\mathrm{W\,m^{-2}}$.

The AWS-assisted ensemble (Fig. 9b) shows a similar annual flux evolution as the posterior ensemble. Compared to the posterior ensemble, Q_{SWnet} in the AWS-assisted ensemble shows larger inter-annual variability, with an earlier and larger increase in the second half of the hydrological year. The albedo time series (Fig. 8e) reveals that this is due to an albedo decay that is closer to the observations from May to September. However, the AWS ensemble generates excessive albedo decay under cold conditions and underestimates Q_{SWnet} in the late melt season due to unaccounted ice exposure. Therefore, the AWS-assisted ensemble does not represent the physical truth but instead the best possible solution given the parameterisations and higher resolution calibration data.

The posterior ensemble consistently underestimates Q_{SWnet} by up to -82 $\mathrm{W\,m^{-2}}$ when considering periods where the AWS-assisted ensemble agrees well with measured albedo. This effect is even larger considering the raw observations. We attribute this difference to the misrepresentation of surface albedo and to an underestimation of Q_{SWin} (Fig. A2, S17). While the AWS-assisted ensemble shows good agreement with observed Q_{LWnet}, the posterior ensemble has a mean difference of 26 $\mathrm{W\,m^{-2}}$ (max. 73 $\mathrm{W\,m^{-2}}$) compared to the AWS-assisted ensemble. This year-round underestimation of Q_{LWnet} offsets the aforementioned Q_{SWnet} discrepancy, and the posterior ensemble receives on average 9.3 $\mathrm{W\,m^{-2}}$ more net radiation.

The posterior ensemble further underestimates the turbulent fluxes during winter and spring, but overestimates them during summer. These deviations peak from August to late September, reaching 34 $\mathrm{W\,m^{-2}}$. The underestimation in the posterior ensemble compared to the AWS-assisted ensemble coincides with a cold bias in AWS-assisted surface temperatures (see Fig. 8c). There is also strong evidence that the surplus of turbulent heat flux in summer is due to an overestimation of humidity, near-surface air temperature, and wind speed in COSMO forcing data (see Fig. A2f and l and Fig. S16). The temperature and humidity biases may also contribute to the overestimation of Q_{LWin}, as they are used in the parameterisation relating cloud cover to Q_{LWin}.

Differences in Q_{R} are negligible since both ensembles use the same precipitation forcing, and the posterior ensemble Q_{G} shows a small negative bias, especially during the late melt season.

The net effect of the energy flux differences on the overall available melt energy is complex. The posterior ensemble shows less available melt energy compared to the AWS-assisted ensemble (max. -32 $\mathrm{W\,m^{-2}}$) in the early summer season (June to mid July), followed by a strong overestimation later in summer with peak deviations up to 109 $\mathrm{W\,m^{-2}}$ related to the albedo overestimation in the AWS-assisted ensemble. Comparing the posterior ensemble net radiation terms to the observations, it is evident that during peak melt season underestimated Q_{SWnet} is counterbalanced by the overestimation of Q_{LWnet} and too large turbulent heat fluxes caused by the biased air temperature and humidity fields. This translates to an underestimation of melt between June and mid July of 0.07 m w.e., while cumulative melt is overestimated over the hydrological year by 0.33 m w.e., in line with the negative mass balance bias identified previously (Section 3.3.1).

https://doi.org/10.5194/egusphere-2025-6249
Preprint. Discussion started: 21 January 2026

4 Discussion

4.1 Parameter plausibility

We consider the quality of our posterior parameter distributions based on previously published results. We note, however, that the optimal parameters are a result of the specific timescale and meteorological conditions, the measurement and optimisation approach, and the model structure used.

The posterior probability of α_{depth} is strongly constrained at the lower boundary of the allowed parameter range, effectively resetting the surface albedo with small snowfall amounts. This may be attributed to either too much available Q_{ME} or too low summer snowfall in the forcing, which occasionally occurs at HEF (e.g., Voordendag et al., 2023). It is comparable to the 3.2 cm found by Oerlemans and Knap (1998) at Morteratschgletscher and the constant 0.001 m w.e. employed in Giesen and Oerlemans (2012). The latter value converts to approximately 0.33 to 2.0 cm depth, assuming snow densities of 50 to 300 kg m^{-3} (Cuffey and Paterson, 2010).

The posteriors of α_{fs}, α_{firn} and α_{ice} are of a similar magnitude to those found in other studies at HEF ((Dirmhirn and Trojer, 1955; Van De Wal et al., 1992; Zolles et al., 2019). For example, Zolles et al. (2019) reported α_{fs} values of 0.86 to 0.9 but a lower α_{firn} of 0.52 to 0.6 in 2012 at HEF. Measuring albedo at HEF across ten days in late summer 1954, Dirmhirn and Trojer (1955) found lower dry fresh snow albedos at 0.82 and α_{firn} ranging from 0.46 (dirty) to 0.63 (clean). Their measured dirty α_{ice} of 0.29 aligns well with our calibrated value, but they also note clean ice albedos of 0.41. These findings are consistent with Van De Wal et al. (1992), who observed very low α_{ice} (0.1 to 0.16) due to dust accumulation and the presence of meltwater, but also higher values (0.3 to 0.4) towards the centre of the tongue, highlighting strong spatial variability.

The calibrated p_{f} (mean = 0.70) is consistent with findings that report a positive precipitation bias in regional climate models over the Alps (Ban et al., 2014, 2020). However, it remains unclear how much of this bias can be attributed to model deficiencies versus observational shortcomings (Kochendorfer et al., 2017; Prein and Gobiet, 2017; Lundquist et al., 2019). While correcting for precipitation biases improves mean daily snowfall, strong biases can remain in snowfall frequency and intensity (Frei et al., 2018). This supports our results, where the calibrated p_{f} corrects for the total precipitation bias, while the low α_{depth} compensates for underestimated snowfall intensity in summer by increasing the albedo of thin snow layers.

The least constrained parameter is $z0_{\mathrm{ice}}$, which contrasts with the high sensitivity at point scale in other studies (e.g., Sauter and Obleitner, 2015). Our posterior range is consistent with values of 1.3 to 5.0 mm found by Van De Wal et al. (1992) and the glacier-scale 3.0 to 6.0 mm derived from a terrestrial laser scanner at HEF (Smith et al., 2020). However, the roughness length at HEF is highly heterogeneous in space and time with values ranging from < 3 mm to > 40 mm and changing rates as large as 0.25 mm per day (Smith et al., 2020; Chambers et al., 2021). This high variability questions the use of a single, constant $z0_{\mathrm{ice}}$ parameter in our model. This holds for many of our model parameters (Brock et al., 2000, 2006; Gurgiser et al., 2013) and restricts the model's ability to capture the full complexity of glacier surface evolution.

While the AWS-assisted ensembles α_{fs} (weighted median = 0.896) shows good agreement to our posterior, the measured albedo timeseries at the AWS sites indicates that our calibrated model's α_{aging} (weighted median = 1.65 days) and α_{firn} (weighted median = 0.54) are likely overestimated. This is evident by a delayed lowering of the surface albedo during summer. In contrast, the AWS-assisted ensemble at the upper station matches the lowering quite closely during summer but overestimates it in winter, indicating that the albedo scheme may be inadequate (Brock et al., 2000; Bougamont et al., 2005).

4.2 Diagnosing model biases

Our results reveal systematic biases in simulated B_{geod} and SLA that cannot be resolved by parameter tuning alone. Drawing upon the measured AWS data (Fig. 8 and A2), we propose the following explanation: The model shows a structural limitation related to the spatial averaging of Q_{SWin} within 20 m elevation bands. By smoothing topographic variability, this method suppresses higher Q_{SWin} inputs received by sun-exposed grid cells (see Fig. S17). This leads to an underestimation of the available Q_{M} and penetrating Q_{SWin} in the early melt season on the glacier tongue. This effect is worsened in Q_{SWnet} (Fig. S18) by the overestimation of albedo decay parameters (α_{aging} and α_{firn}), leading to the systematic underestimation of the meltout date and thus a delay in the simulated rise of the SLA. These processes may be exacerbated by other model limitations related to the snow settling or the forcing data distribution and snowfall derivation.

Since the satellite observations are predominantly available in winter, the information on these albedo decay related parameters was limited, as confirmed by the small positive bias in simulated $\bar{\alpha}$. To compensate for this artificially slow melt, the calibration process reduces p_{f}, which in turn partly drives the strong negative bias in the modelled B_{geod}. This central offset is a direct consequence of the multi-objective calibration and the conflicting inferences from the different datasets. While a higher p_{f} would correct the bias in the modelled mass balance, such a change is penalised by the SLA and $\bar{\alpha}$ log-likelihoods, which favour a lower precipitation input to match their respective observations.

The resulting posterior therefore represents a compromise solution. The negative mass balance bias at the glacier-scale is a direct consequence of these model and forcing errors that the calibration cannot account for (Günther et al., 2019). Given tight constraints on the albedo evolution enforced by the provided per-pixel and glacier-integrated albedo and snowline observations, the model forced by COSMO-CLM is unable to find a perfect solution fulfilling all three observational constraints.

The initial energy deficit at the glacier surface by the underestimated Q_{SWnet} is offset at the annual scale by overestimated energy inputs from Q_{LWin} and the turbulent fluxes. The systematic nature of the Q_{LWin} bias is particularly detrimental for an accurate simulation of the SEB and surface temperatures (Lapo et al., 2015; Raleigh et al., 2015). This is enhanced by the consistent, unmodulated nature in comparison to Q_{SWin} and the complex interaction with various parts of the SEB (Sauter and Obleitner, 2015; Raleigh et al., 2016; Conway and Cullen, 2016; Conway et al., 2022). This effect can be exacerbated because an underestimated T_{s} can enhance atmospheric stability, and an overeager stability correction may suppress turbulent heat exchange (Slater et al., 2001; Lapo et al., 2015; Raleigh et al., 2016). However, we find that COSMO-CLM's overestimation of T_2 and specific humidity (Fig. S19) during the later ablation season leads to overestimated turbulent fluxes in COSIPY (Fig. S20) and Q_{LWin} (see Fig. A2 and S17). Therefore, while the initial delayed SLA rise is caused by too low Q_{SWnet} because of aforementioned reasons, the overall negative annual mass balance bias is a direct consequence of overestimated Q_{LWin} (year-round) and turbulent heat fluxes, especially during peak melt season.

The connected biases in the turbulent fluxes and Q_{LWin} likely stem from the model's coarse 2.2 km horizontal grid spacing, which is insufficient to resolve the specific microclimate of the glacier boundary layer and its shallow katabatic flow (Goger

https://doi.org/10.5194/egusphere-2025-6249
Preprint. Discussion started: 21 January 2026

et al., 2022; Draeger et al., 2024; Nicholson et al., 2025). In reality, this boundary layer tends to decouple the glacier surface from the warmer, moister ambient atmosphere in summer (e.g., Mott et al., 2020). By failing to resolve this stable boundary layer, COSMO-CLM likely simulates stronger vertical mixing, thereby enhancing the exchange of warmer and humid air between the overlying atmosphere and the glacier surface. This process is likely compounded by an inaccurate representation of the glacier surface and the parameter choices within the land surface scheme, and may be enhanced by an overestimated simulated cloud cover.

Indeed, trying to tune the b parameter in Equation 8 (see e.g., Conway et al., 2022) still results in a substantial bias that can only be reduced by strongly adjusting ϵ_{cl} or employing a cloud cover correction factor (not shown). These findings highlight the paramount need for accurate climatological forcing and downscaling measures to advance process-based glacier modelling. We did not include the parameters of the Q_{LWin} parameterisation into our framework, but the employed calibration and model chain shows the diagnostic abilities to help identify such forcing biases. Such a calibration framework can thus be a useful tool to diagnose inconsistencies in the model chain and can help bias-adjust climatological data as more observations become available. The well-constrained systematic error terms support this.

4.3 Future research

While we have shown that an SEB model can be calibrated using exclusively globally available remote observations and high-resolution climate model data in place of scarce in situ measurements, limitations regarding the performance and transferability of this study arise. We have split these caveats into three parts: limitations related to the forcing data, those related to structural model errors including process representation and those related to the methodological design.

First, the underlying assumption in our study is that the atmospheric forcing data and intermediate steps such as the surrogate model development or forcing data extrapolation are flawless. The exception is total precipitation, which is corrected in COSIPY with a constant p_{f}. In reality, forcing uncertainty is often the largest contributor to SEB variance (Günther et al., 2019). Our results show that calibrated parameters are tightly linked to the biases in COSMO-CLMs air temperature, humidity, Q_{LWin} and Q_{SWin}. While we did not investigate accumulation mechanisms, other studies highlight the critical role of accurate precipitation timing beyond the seasonal scale and a simple bias correction (Johnson and Rupper, 2020; Shaw et al., 2025). Future implementations may also benefit from more advanced solid precipitation fractionation schemes, which can have a strong impact on snowpack simulations (Günther et al., 2019; Jennings and Molotch, 2019; Bernat et al., 2025). Following the results of Vionnet et al. (2022), a better parameterisation would be a wet-bulb scheme (e.g., Ding et al., 2017; Buri et al., 2023) or incorporating vertical atmospheric profiles as resolved by high-resolution CPM. In the absence of additional observations, accurately accounting for these parameters and the aforementioned biases at unmonitored glaciers remains a key challenge.

Second, COSIPY is limited by structural simplifications, including the lack of a representation for debris cover and snow redistribution and the application of linear lapse rates (Voordendag et al., 2024; Zhu et al., 2024), as evidenced by the mismatches between observed and simulated mass balance gradients. New developments in the parameterisation of these processes (Saigger et al., 2024) and the advent of online-coupled glacier-atmosphere models at resolutions on the hectometer scale offer exciting opportunities to address these limitations (Collier and Immerzeel, 2015; Bonekamp et al., 2019; Reynolds et al., 2024). Yet,

https://doi.org/10.5194/egusphere-2025-6249
Preprint. Discussion started: 21 January 2026

even at these scales, exchanges between the glacier and the atmosphere and complex boundary-layer phenomena like katabatic winds may not be accurately reflected (Goger et al., 2022; Draeger et al., 2024). In addition, we find that even the AWS-assisted ensemble cannot match the observed albedo evolution, indicating that the employed parameterisation is inadequate.

Third, parameters are assumed to be constant in time and space. Several studies show that optimal parameter values vary with local climatic settings and surface characteristics (Gurgiser et al., 2013; Prinz et al., 2016; Galos et al., 2017; Zolles et al., 2019; Zolles and Born, 2021). Additionally, we neglected the covariance between the observational datasets which leads to an underestimation of the uncertainty in the posterior parameter distributions. This issue is compounded by the higher availability of satellite observations with less cloudy and thus often winter and snow-covered conditions that provide insufficient guidance for melt-related parameters. This framework will scale well with advancements in climate models and data availability, particularly from high-temporal and spatial-resolution satellite missions (Scher et al., 2021; Falaschi et al., 2023; Jiao et al., 2025) or their synthesis toward spatially resolved mass balances (Miles et al., 2021; Kneib et al., 2024).

Data assimilation in glaciology is a growing field (Morlighem and Goldberg, 2023), and different assimilation schemes can better address the temporal variability of model parameters (e.g., Landmann et al., 2021) at the cost of a reduced uncertainty exploration. We consider this a lower priority compared to the adverse conditions created by forcing biases and structural simplifications. If anything, our results indicate that choosing fixed observed albedo constants, but allowing for the calibration of forcing bias correction parameters, may be more beneficial for the application at unmonitored glaciers. Although not explicitly quantified, the impact of parameter uncertainty is small compared to that of the forcing data, except when a parameter set triggers a premature or delayed bare ice exposure. Indeed, inspecting the ensemble spread induced by the parameter choice versus the bias between observed and simulated net radiation emphasises the smaller role of parametric uncertainty. While the strong data inference may warrant that a more simplistic uncertainty quantification, as obtained by a state estimation method, is sufficient, another compromise could be the use of a hierarchical Bayesian model. Such a model could better use the varying temporal resolution of the observations. While the long-term geodetic mass balance target could constrain the hyperparameters of a common top-level distribution, higher frequency snowline and albedo observations would then inform each year's specific parameters. This would provide a fallback estimate from the common parameter pool in years where high-frequency observations are sparse. Applying such a framework at other glaciers or larger scales requires a new surrogate per glacier, as the training data required to account for variable forcing and parameters is too large. We find that this can be achieved with approximately 1000 LHS iterations (see Fig. S13), enabling such a calibration framework at manageable computational cost.

Given the high demand for accurate forcing data and the potential for compounding errors, it remains unclear whether this physically-based calibration allows for an accurate assessment of the individual energy fluxes when forcing biases are unknown. Nevertheless, the calibration reproduces the interannual mass balance variability well. This indicates that, even though compensating errors exist among the flux components and also along the elevational gradient, the model chain correctly captures the overall glacier-wide response to atmospheric variability. This is a promising result for improving our understanding of the atmospheric drivers at unmonitored glaciers. In addition, the demonstrated ability to diagnose errors within the model chain suggests that including additional bias correction terms may be possible, in the same way as the p_{f} is included as a tuning parameter.

https://doi.org/10.5194/egusphere-2025-6249
Preprint. Discussion started: 21 January 2026

5 Conclusion

Motivated by the paucity of in-situ surface energy balance measurements for most glaciers worldwide, this study developed and evaluated a Bayesian calibration framework for a physically based SEB model using only globally available satellite data and high-resolution climate simulations. By combining a multi-objective MCMC calibration with surrogate models, we achieved robust parameter estimates and quantified their uncertainty at otherwise prohibitive computational cost. The applicability of such surrogates provides an exciting avenue for future research, and the calibration yields robust estimates for parameter values and their uncertainty. Our study provides several findings:

- Within COSIPY, and likely other SEB models, parameter equifinality arises mainly among the precipitation factor and albedo decay-related parameters such as albedo aging and firn albedo. These parameters remain difficult to constrain without in-situ data, but higher frequency remotely sensed observations could help address this.

- The surface energy balance uncertainty introduced by parameter choices is small unless parameter sets shift the timing of snow melt-out. Parameter uncertainty itself is tightly constrained and flux variations introduced by errors in the meteorological forcing generally exceed their sensitivity. Therefore, it is paramount to improve the representation of the near-surface boundary layer, (solid) precipitation, humidity and cloud cover in high-resolution climate simulations in complex terrain. Such efforts would also benefit from (meteorological) glacier observation databases to better identify accurate parameterisations and forcing biases.

- The calibration reveals inconsistencies between long-term mass budgets and higher frequency snow-cover or albedo observations. This diagnostic capability could help identify and be extended to include explicit forcing bias corrections as more observations become available. In turn, with reliable forcing, a model calibrated this way provides a physically consistent flux partitioning. This provides further motivation to develop non-stationary parameterisations that could be more robust under changing climate conditions.

- The remote-only calibration reproduces the observed interannual mass balance variability and glacier mean albedos, but shows a delayed snowline rise and a negative mass balance bias. This can be explained by initially too low net shortwave radiation in the early melt-season, which is offset at the annual scale by excessive incoming longwave radiation and turbulent fluxes. We find that the uncertainty-aware calibration can capture the glacier response to changing atmospheric conditions. When meteorological biases are known, the same framework can also provide robust estimates of the surface energy balance. This workflow circumvents the need for in-situ data to calibrate model parameters, and enables physically based glacier modelling in remote regions at the cost of higher computational demand.

Notwithstanding its limitations, this study provides a robust and transferable parameter calibration framework for unmonitored glaciers, capable of reproducing the interannual mass balance variability. While parameter choice and its associated uncertainty are a tractable challenge, forcing uncertainty remains the main obstacle to the application of surface energy balance models for remote-only applications. The presented framework offers diagnostic capabilities to help identify shortcomings and inconsistencies between model parameters, model structure and forcing, paving the way for also including forcing bias corrections

https://doi.org/10.5194/egusphere-2025-6249
Preprint. Discussion started: 21 January 2026

when more observations become available.

Without prior knowledge of the forcing quality, this raises questions about whether a remote-only surface energy balance model calibration can reliably diagnose the individual energy balance fluxes or if the model appears plausible while misrepresenting the underlying physical processes. Nevertheless, the framework successfully reproduces the interannual mass balance variability, indicating that it captures the overall glacier-wide response to atmospheric variability even when individual fluxes are biased. Conversely, knowledge of well-established parameters or the inclusion of additional bias correction or downscaling parameters in such a Bayesian framework can serve to detect and correct forcing biases. We conclude that a comprehensive assessment of forcing data uncertainty is essential for advancing process-based glacier modelling in unmonitored regions and at larger scales. By addressing these limitations, surface energy balance models can be enabled as powerful tools for robust, large-scale assessments of glacier–atmosphere interactions in unmonitored regions.

Appendix A: Additional figures

https://doi.org/10.5194/egusphere-2025-6249
Preprint. Discussion started: 21 January 2026

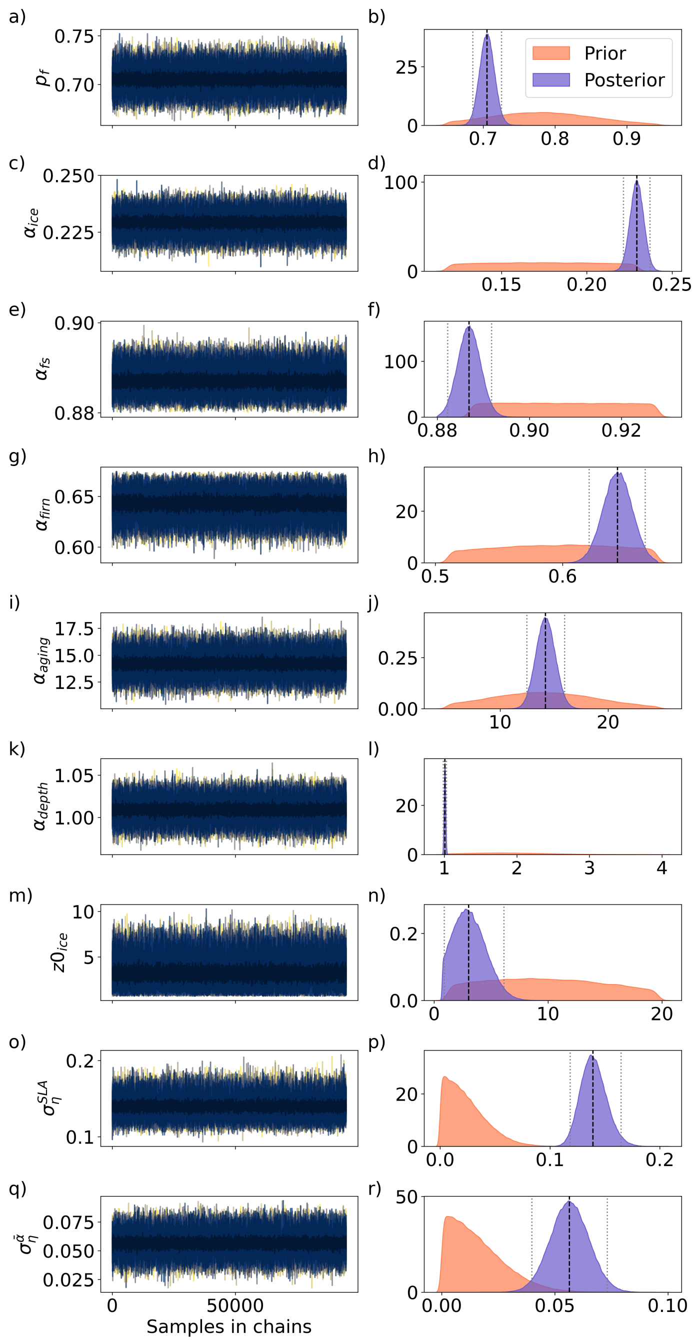

Figure A1. Traces (left) and prior and posterior marginal distributions (right) of the model parameters and systematic errors in orange and blue, respectively. The black lines in the traces correspond to the mean across the fifteen chains.

https://doi.org/10.5194/egusphere-2025-6249
Preprint. Discussion started: 21 January 2026

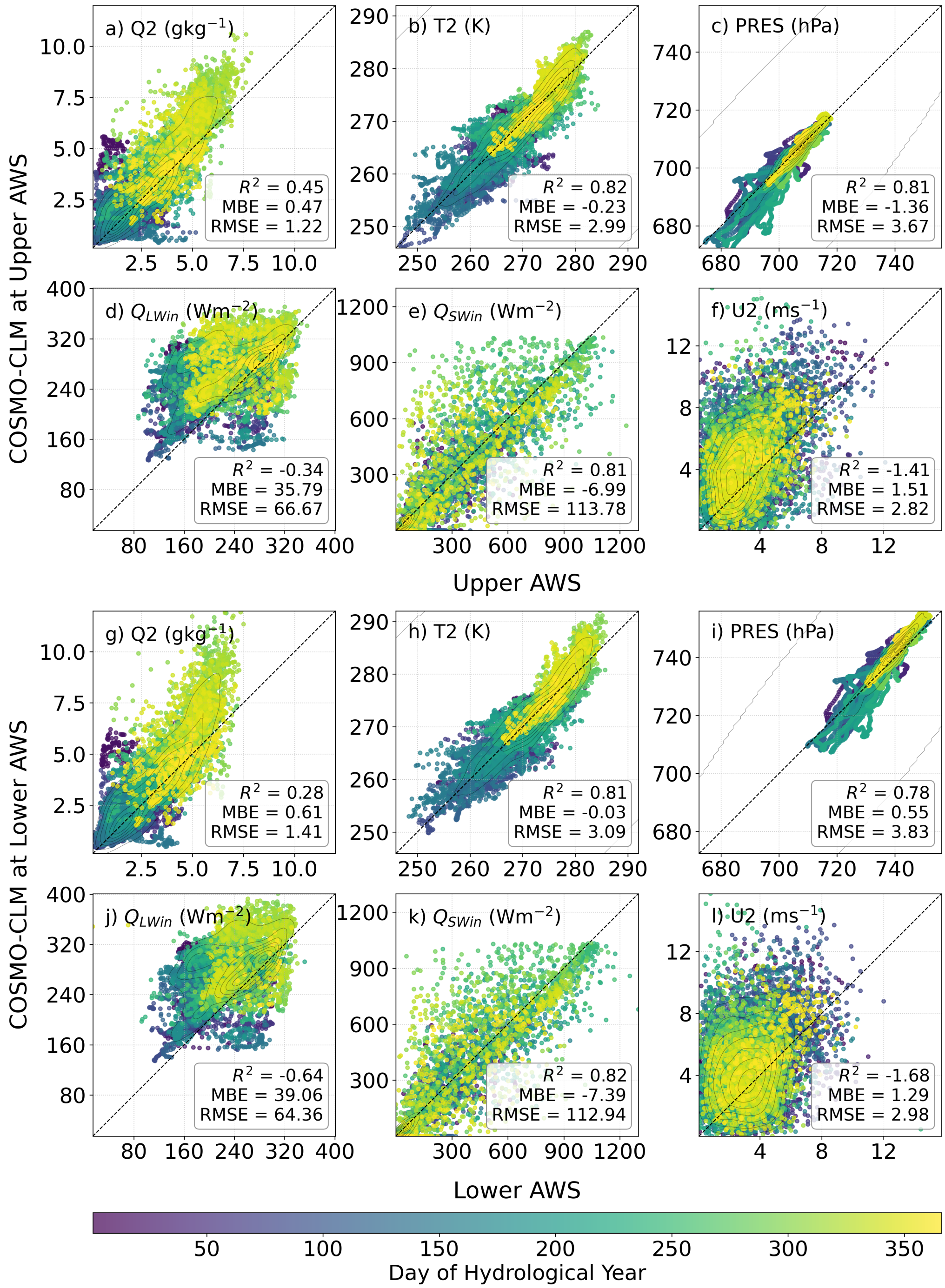

Figure A2. Scatterplot of all input variables except for total precipitation at the upper and lower station in comparison to the nearest COSIPY grid cell. To isolate the moisture signal in the relative humidity input, we instead display the specific humidity (Q2). The contour lines represent the data density, and points are colored based on the day of the year in the hydrological year 2003/04. Metrics refer to the coefficient of determination R^2, the mean bias error (MBE) and the root mean squared error (RMSE) in the respective units.

Code and data availability. The model code is based on the open-source COSIPY model (https://github.com/cryotools/cosipy, last accessed: 04.11.2025). The adapted COSIPY code used within this paper and the subsequent analysis is freely accessible via Zenodo at https://doi.org/10.5281/zenodo.17426863 (Richter, 2025). As output file sizes are quite large, they are available upon request. The COSMO-CLM simulations are available from the ESGF (https://esgf-ui.ceda.ac.uk/search, last accessed: 04.11.2025). Access to the calibration data and the required code can be found in Hugonnet et al. (2021), Ren et al. (2024), and Loibl et al. (2025), respectively.

Author contributions. NR, LN and FM conceptualised the research, while NR, NU and MS developed the calibration framework. NR performed the formal analysis and created the visualisations, and RP provided guidance for the data usage at Hintereisferner. AA and NG contributed to software development, and NB helped access and analyse the forcing data. LN contributed to all stages of the research and provided supervision. All authors contributed to the preparation of the manuscript.

Competing interests. The contact author has declared that none of the authors has any competing interests.

Acknowledgements. We thank Friedrich Obleitner for providing the automatic weather station data, Shaoting Ren for providing the script routine to calculate the Landsat albedo and Lilian Schuster, Emily Collier and Codruț-Andrei Diaconu for valuable discussions. Long-term funding of monitoring and infrastructure at Hintereisferner is provided by the Federal State of Tyrol, Austria (Department of Hydrography and Hydrology) and the University of Innsbruck. Computational resources were gratefully received from the Cirrus high-performance computing cluster of the Geography Department of Humboldt-Universität zu Berlin. Nikolina Ban acknowledges PRACE for awarding access to Piz Daint at Swiss National Supercomputing Center (CSCS, Switzerland), and the Federal Office for Meteorology and Climatology MeteoSwiss, the Swiss National Supercomputing Centre (CSCS), and ETH Zürich for their contributions to the development of the GPU-accelerated version of COSMO. Niklas Richter received funding from the doctoral scholarship provided by the University of Innsbruck. Matthias Scheiter was supported by the Australian Research Council Special Research Initiative, Australian Centre for Excellence in Antarctic Science (Project Number SR200100008). Generative AI was used to help with coding and correct spelling in this manuscript.

https://doi.org/10.5194/egusphere-2025-6249
Preprint. Discussion started: 21 January 2026

References

Abermann, J., Kinnard, C., and MacDonell, S.: Albedo variations and the impact of clouds on glaciers in the Chilean semi-arid Andes, Journal of Glaciology, 60, 183–191, https://doi.org/10.3189/2014JoG13J094, 2014.

Abril-Pla, O., Andreani, V., Carroll, C., Dong, L., Fonnesbeck, C. J., Kochurov, M., Kumar, R., Lao, J., Luhmann, C. C., Martin, O. A., Osthege, M., Vieira, R., Wiecki, T., and Zinkov, R.: PyMC: a modern, and comprehensive probabilistic programming framework in Python, PeerJ Computer Science, 9, e1516, https://doi.org/10.7717/peerj-cs.1516, 2023.

Aguayo, R., Maussion, F., Schuster, L., Schaefer, M., Caro, A., Schmitt, P., Mackay, J., Ultee, L., Leon-Muñoz, J., and Aguayo, M.: Unravelling the sources of uncertainty in glacier runoff projections in the Patagonian Andes (40–56° S), The Cryosphere, 18, 5383–5406, https://doi.org/10.5194/tc-18-5383-2024, 2024.

Arndt, A. and Schneider, C.: Spatial pattern of glacier mass balance sensitivity to atmospheric forcing in High Mountain Asia, Journal of Glaciology, pp. 1–18, https://doi.org/10.1017/jog.2023.46, 2023.

Arndt, A., Scherer, D., and Schneider, C.: Atmosphere Driven Mass-Balance Sensitivity of Halji Glacier, Himalayas, Atmosphere, 12, 426, https://doi.org/10.3390/atmos12040426, 2021.

Aschwanden, A. and Brinkerhoff, D. J.: Calibrated Mass Loss Predictions for the Greenland Ice Sheet, Geophysical Research Letters, 49, e2022GL099 058, https://doi.org/10.1029/2022GL099058, 2022.

Baldauf, M., Seifert, A., Förstner, J., Majewski, D., Raschendorfer, M., and Reinhardt, T.: Operational Convective-Scale Numerical Weather Prediction with the COSMO Model: Description and Sensitivities, Monthly Weather Review, 139, 3887–3905, https://doi.org/10.1175/MWR-D-10-05013.1, 2011.

Ban, N., Schmidli, J., and Schär, C.: Evaluation of the convection-resolving regional climate modeling approach in decade-long simulations, Journal of Geophysical Research: Atmospheres, 119, 7889–7907, https://doi.org/10.1002/2014JD021478, 2014.

Ban, N., Rajczak, J., Schmidli, J., and Schär, C.: Analysis of Alpine precipitation extremes using generalized extreme value theory in convection-resolving climate simulations, Climate Dynamics, 55, 61–75, https://doi.org/10.1007/s00382-018-4339-4, 2020.

Ban, N., Caillaud, C., Coppola, E., Pichelli, E., Sobolowski, S., Adinolfi, M., Ahrens, B., Alias, A., Anders, I., Bastin, S., Belušić, D., Berthou, S., Brisson, E., Cardoso, R. M., Chan, S. C., Christensen, O. B., Fernández, J., Fita, L., Frisius, T., Gašparac, G., Giorgi, F., Goergen, K., Haugen, J. E., Hodnebrog, , Kartsios, S., Katragkou, E., Kendon, E. J., Keuler, K., Lavin-Gullon, A., Lenderink, G., Leutwyler, D., Lorenz, T., Maraun, D., Mercogliano, P., Milovac, J., Panitz, H.-J., Raffa, M., Remedio, A. R., Schär, C., Soares, P. M. M., Srnec, L., Steensen, B. M., Stocchi, P., Tölle, M. H., Truhetz, H., Vergara-Temprado, J., De Vries, H., Warrach-Sagi, K., Wulfmeyer, V., and Zander, M. J.: The first multi-model ensemble of regional climate simulations at kilometer-scale resolution, part I: evaluation of precipitation, Climate Dynamics, 57, 275–302, https://doi.org/10.1007/s00382-021-05708-w, 2021.

Barandun, M., Huss, M., Usubaliev, R., Azisov, E., Berthier, E., Kääb, A., Bolch, T., and Hoelzle, M.: Multi-decadal mass balance series of three Kyrgyz glaciers inferred from modelling constrained with repeated snow line observations, The Cryosphere, 12, 1899–1919, https://doi.org/10.5194/tc-12-1899-2018, 2018.

Bernat, M., Miles, E. S., Kneib, M., Fujita, K., Sasaki, O., Shaw, T. E., and Pellicciotti, F.: Precipitation phase drives seasonal and decadal snowline changes in high mountain Asia, Environmental Research Letters, 20, 064 039, https://doi.org/10.1088/1748-9326/adcf39, 2025.

Berthier, E., Floriciou, D., Gardner, A. S., Gourmelen, N., Jakob, L., Paul, F., Treichler, D., Wouters, B., Belart, J. M. C., Dehecq, A., Dussaillant, I., Hugonnet, R., Kääb, A., Krieger, L., Pálsson, F., and Zemp, M.: Measuring glacier mass changes from space—a review, Reports on Progress in Physics, 86, 036 801, https://doi.org/10.1088/1361-6633/acaf8e, 2023.

https://doi.org/10.5194/egusphere-2025-6249
Preprint. Discussion started: 21 January 2026

Bintanja, R. and Van Den Broeke, M. R.: The Surface Energy Balance of Antarctic Snow and Blue Ice, Journal of Applied Meteorology, 34, 902–926, https://doi.org/10.1175/1520-0450(1995)034<0902:TSEBOA>2.0.CO;2, 1995.

Blau, M. T., Turton, J. V., Sauter, T., and Mölg, T.: Surface mass balance and energy balance of the 79N Glacier (Nioghalvfjerdsfjorden, NE Greenland) modeled by linking COSIPY and Polar WRF, Journal of Glaciology, 67, 1093–1107, https://doi.org/10.1017/jog.2021.56, 2021.

Bonekamp, P. N. J., De Kok, R. J., Collier, E., and Immerzeel, W. W.: Contrasting Meteorological Drivers of the Glacier Mass Balance Between the Karakoram and Central Himalaya, Frontiers in Earth Science, 7, 107, https://doi.org/10.3389/feart.2019.00107, 2019.

Bougamont, M., Bamber, J. L., and Greuell, W.: A surface mass balance model for the Greenland Ice Sheet, Journal of Geophysical Research: Earth Surface, 110, 2005JF000 348, https://doi.org/10.1029/2005JF000348, 2005.

Braithwaite, R. J., Raper, S. C., and Candela, R.: Recent changes (1991–2010) in glacier mass balance and air temperature in the European Alps, Annals of Glaciology, 54, 139–146, https://doi.org/10.3189/2013AoG63A285, 2013.

Brock, B. W., Willis, I. C., and Sharp, M. J.: Measurement and parameterization of albedo variations at Haut Glacier d'Arolla, Switzerland, Journal of Glaciology, 46, 675–688, https://doi.org/10.3189/172756500781832675, 2000.

Brock, B. W., Willis, I. C., and Sharp, M. J.: Measurement and parameterization of aerodynamic roughness length variations at Haut Glacier d'Arolla, Switzerland, Journal of Glaciology, 52, 281–297, https://doi.org/10.3189/172756506781828746, 2006.

Brun, F., Dumont, M., Wagnon, P., Berthier, E., Azam, M. F., Shea, J. M., Sirguey, P., Rabatel, A., and Ramanathan, A.: Seasonal changes in surface albedo of Himalayan glaciers from MODIS data and links with the annual mass balance, The Cryosphere, 9, 341–355, https://doi.org/10.5194/tc-9-341-2015, 2015.

Buri, P., Fatichi, S., Shaw, T. E., Miles, E. S., McCarthy, M. J., Fyffe, C. L., Fugger, S., Ren, S., Kneib, M., Jouberton, A., Steiner, J., Fujita, K., and Pellicciotti, F.: Land Surface Modeling in the Himalayas: On the Importance of Evaporative Fluxes for the Water Balance of a High-Elevation Catchment, Water Resources Research, 59, e2022WR033 841, https://doi.org/10.1029/2022WR033841, 2023.

Buri, P., Fatichi, S., Shaw, T. E., Fyffe, C. L., Miles, E. S., McCarthy, M. J., Kneib, M., Ren, S., Jouberton, A., Fugger, S., Jia, L., Zhang, J., Shen, C., Zheng, C., Menenti, M., and Pellicciotti, F.: Land surface modeling informed by earth observation data: toward understanding blue–green–white water fluxes in High Mountain Asia, Geo-spatial Information Science, pp. 1–25, https://doi.org/10.1080/10095020.2024.2330546, 2024.

Chambers, J. R., Smith, M. W., Smith, T., Sailer, R., Quincey, D. J., Carrivick, J. L., Nicholson, L., Mertes, J., Stiperski, I., and James, M. R.: Correcting for Systematic Underestimation of Topographic Glacier Aerodynamic Roughness Values From Hintereisferner, Austria, Frontiers in Earth Science, 9, 691 195, https://doi.org/10.3389/feart.2021.691195, 2021.

Chen, J., Du, W., Kang, S., Qin, X., Sun, W., Liu, Y., Luo, L., He, J., Jiang, Y., and Sun, W.: Comparison of energy and mass balance characteristics between two glaciers in adjacent basins in the Qilian Mountains, Climate Dynamics, 61, 1535–1550, https://doi.org/10.1007/s00382-022-06641-2, 2023.

Cogley, J. G., Hock, R., Rasmussen, L. A., Arendt, A. A., Bauder, A., Braithwaite, R. J., Jansson, P., Kaser, G., Möller, M., Nicholson, L., and Zemp, M.: Glossary of glacier mass balance and related terms, Int. Assoc. Cryospheric Sci., https://doi.org/10.5167/UZH-53475, publisher: UNESCO/IHP, 2011.

Collier, E. and Immerzeel, W. W.: High-resolution modeling of atmospheric dynamics in the Nepalese Himalaya, Journal of Geophysical Research: Atmospheres, 120, 9882–9896, https://doi.org/10.1002/2015JD023266, 2015.

Collier, E., Mölg, T., Maussion, F., Scherer, D., Mayer, C., and Bush, A. B. G.: High-resolution interactive modelling of the mountain glacier–atmosphere interface: an application over the Karakoram, The Cryosphere, 7, 779–795, https://doi.org/10.5194/tc-7-779-2013, 2013.

Conway, J. P. and Cullen, N. J.: Cloud effects on surface energy and mass balance in the ablation area of Brewster Glacier, New Zealand, The Cryosphere, 10, 313–328, https://doi.org/10.5194/tc-10-313-2016, 2016.

Conway, J. P., Abermann, J., Andreassen, L. M., Azam, M. F., Cullen, N. J., Fitzpatrick, N., Giesen, R. H., Langley, K., MacDonell, S., Mölg, T., Radić, V., Reijmer, C. H., and Sicart, J.-E.: Cloud forcing of surface energy balance from in situ measurements in diverse mountain glacier environments, The Cryosphere, 16, 3331–3356, https://doi.org/10.5194/tc-16-3331-2022, 2022.

Cook, D., Malinauskaite, L., Davíðsdóttir, B., and Ögmundardóttir, H.: Co-production processes underpinning the ecosystem services of glaciers and adaptive management in the era of climate change, Ecosystem Services, 50, 101 342, https://doi.org/10.1016/j.ecoser.2021.101342, 2021.

Coppola, E., Sobolowski, S., Pichelli, E., Raffaele, F., Ahrens, B., Anders, I., Ban, N., Bastin, S., Belda, M., Belusic, D., Caldas-Alvarez, A., Cardoso, R. M., Davolio, S., Dobler, A., Fernandez, J., Fita, L., Fumiere, Q., Giorgi, F., Goergen, K., Güttler, I., Halenka, T., Heinzeller, D., Hodnebrog, , Jacob, D., Kartsios, S., Katragkou, E., Kendon, E., Khodayar, S., Kunstmann, H., Knist, S., Lavín-Gullón, A., Lind, P., Lorenz, T., Maraun, D., Marelle, L., Van Meijgaard, E., Milovac, J., Myhre, G., Panitz, H.-J., Piazza, M., Raffa, M., Raub, T., Rockel, B., Schär, C., Sieck, K., Soares, P. M. M., Somot, S., Srnec, L., Stocchi, P., Tölle, M. H., Truhetz, H., Vautard, R., De Vries, H., and Warrach-Sagi, K.: A first-of-its-kind multi-model convection permitting ensemble for investigating convective phenomena over Europe and the Mediterranean, Climate Dynamics, 55, 3–34, https://doi.org/10.1007/s00382-018-4521-8, 2020.

Cremona, A., Huss, M., Landmann, J. M., Schwaizer, G., Paul, F., and Farinotti, D.: Constraining sub-seasonal glacier mass balance in the Swiss Alps using Sentinel-2-derived snow-cover observations, Journal of Glaciology, 71, e25, https://doi.org/10.1017/jog.2025.1, 2025.

Cuffey, K. M. and Paterson, W. S. B.: The physics of glaciers, Elsevier, San Diego, fourth edition edn., ISBN 978-0-12-369461-4 978-0-08-091912-6, 2010.

Dee, D. P., Uppala, S. M., Simmons, A. J., Berrisford, P., Poli, P., Kobayashi, S., Andrae, U., Balmaseda, M. A., Balsamo, G., Bauer, P., Bechtold, P., Beljaars, A. C. M., Van De Berg, L., Bidlot, J., Bormann, N., Delsol, C., Dragani, R., Fuentes, M., Geer, A. J., Haimberger, L., Healy, S. B., Hersbach, H., Hólm, E. V., Isaksen, L., Kållberg, P., Köhler, M., Matricardi, M., McNally, A. P., Monge-Sanz, B. M., Morcrette, J., Park, B., Peubey, C., De Rosnay, P., Tavolato, C., Thépaut, J., and Vitart, F.: The ERA-Interim reanalysis: configuration and performance of the data assimilation system, Quarterly Journal of the Royal Meteorological Society, 137, 553–597, https://doi.org/10.1002/qj.828, 2011.

Ding, B., Yang, K., Yang, W., He, X., Chen, Y., Lazhu, Guo, X., Wang, L., Wu, H., and Yao, T.: Development of a Water and Enthalpy Budget-based Glacier mass balance Model (WEB-GM) and its preliminary validation, Water Resources Research, 53, 3146–3178, https://doi.org/10.1002/2016WR018865, 2017.

Dirmhirn, I. and Trojer, E.: Albedountersuchungen auf dem Hintereisferner, Archiv für Meteorologie, Geophysik und Bioklimatologie Serie B, 6, 400–416, https://doi.org/10.1007/BF02242745, 1955.

Draeger, C., Radić, V., White, R. H., and Tessema, M. A.: Evaluation of reanalysis data and dynamical downscaling for surface energy balance modeling at mountain glaciers in western Canada, The Cryosphere, 18, 17–42, https://doi.org/10.5194/tc-18-17-2024, 2024.

Dumont, M., Durand, Y., Arnaud, Y., and Six, D.: Variational assimilation of albedo in a snowpack model and reconstruction of the spatial mass-balance distribution of an alpine glacier, Journal of Glaciology, 58, 151–164, https://doi.org/10.3189/2012JoG11J163, 2012.

https://doi.org/10.5194/egusphere-2025-6249
Preprint. Discussion started: 21 January 2026

Essery, R., Morin, S., Lejeune, Y., and B Ménard, C.: A comparison of 1701 snow models using observations from an alpine site, Advances in Water Resources, 55, 131–148, https://doi.org/10.1016/j.advwatres.2012.07.013, 2013.

Falaschi, D., Bhattacharya, A., Guillet, G., Huang, L., King, O., Mukherjee, K., Rastner, P., Yao, T., and Bolch, T.: Annual to seasonal glacier mass balance in High Mountain Asia derived from Pléiades stereo images: examples from the Pamir and the Tibetan Plateau, The Cryosphere, 17, 5435–5458, https://doi.org/10.5194/tc-17-5435-2023, 2023.

Farinotti, D., Huss, M., Fürst, J. J., Landmann, J., Machguth, H., Maussion, F., and Pandit, A.: A consensus estimate for the ice thickness distribution of all glaciers on Earth, Nature Geoscience, 12, 168–173, https://doi.org/10.1038/s41561-019-0300-3, 2019.

Fitzpatrick, N., Radić, V., and Menounos, B.: Surface Energy Balance Closure and Turbulent Flux Parameterization on a Mid-Latitude Mountain Glacier, Purcell Mountains, Canada, Frontiers in Earth Science, 5, 67, https://doi.org/10.3389/feart.2017.00067, 2017.

Fosser, G., Gaetani, M., Kendon, E. J., Adinolfi, M., Ban, N., Belušić, D., Caillaud, C., Careto, J. A. M., Coppola, E., Demory, M.-E., De Vries, H., Dobler, A., Feldmann, H., Goergen, K., Lenderink, G., Pichelli, E., Schär, C., Soares, P. M. M., Somot, S., and Tölle, M. H.: Convection-permitting climate models offer more certain extreme rainfall projections, npj Climate and Atmospheric Science, 7, 51, https://doi.org/10.1038/s41612-024-00600-w, 2024.

Frederikse, T., Landerer, F., Caron, L., Adhikari, S., Parkes, D., Humphrey, V. W., Dangendorf, S., Hogarth, P., Zanna, L., Cheng, L., and Wu, Y.-H.: The causes of sea-level rise since 1900, Nature, 584, 393–397, https://doi.org/10.1038/s41586-020-2591-3, 2020.

Frei, P., Kotlarski, S., Liniger, M. A., and Schär, C.: Future snowfall in the Alps: projections based on the EURO-CORDEX regional climate models, The Cryosphere, 12, 1–24, https://doi.org/10.5194/tc-12-1-2018, 2018.

Fugazza, D., Senese, A., Azzoni, R. S., Maugeri, M., and Diolaiuti, G. A.: Spatial distribution of surface albedo at the Forni Glacier (Stelvio National Park, Central Italian Alps), Cold Regions Science and Technology, 125, 128–137, https://doi.org/10.1016/j.coldregions.2016.02.006, 2016.

Furian, W., Maussion, F., and Schneider, C.: Projected 21st-Century Glacial Lake Evolution in High Mountain Asia, Frontiers in Earth Science, 10, 821 798, https://doi.org/10.3389/feart.2022.821798, 2022.

Gabbi, J., Carenzo, M., Pellicciotti, F., Bauder, A., and Funk, M.: A comparison of empirical and physically based glacier surface melt models for long-term simulations of glacier response, Journal of Glaciology, 60, 1140–1154, https://doi.org/10.3189/2014JoG14J011, 2014.

Galos, S. P., Klug, C., Maussion, F., Covi, F., Nicholson, L., Rieg, L., Gurgiser, W., Mölg, T., and Kaser, G.: Reanalysis of a 10-year record (2004–2013) of seasonal mass balances at Langenferner/Vedretta Lunga, Ortler Alps, Italy, The Cryosphere, 11, 1417–1439, https://doi.org/10.5194/tc-11-1417-2017, 2017.

Gao, Y., Chen, F., and Jiang, Y.: Evaluation of a Convection-Permitting Modeling of Precipitation over the Tibetan Plateau and Its Influences on the Simulation of Snow-Cover Fraction, Journal of Hydrometeorology, 21, 1531–1548, https://doi.org/10.1175/JHM-D-19-0277.1, 2020.

GAPHAZ: Assessment of Glacier and Permafrost Hazards in Mountain Regions - Technical Guidance Document, Standing Group on Glacier and Permafrost Hazards in Mountains (GAPHAZ) of the International Association of Cryospheric Sciences (IACS) and the International Permafrost Association (IPA), Zurich, Switzerland and Lima, Peru, 2017.

Gastaldello, M., Mattea, E., Hoelzle, M., and Machguth, H.: Modelling cold firn evolution at Colle Gnifetti, Swiss/Italian Alps, The Cryosphere, 19, 2983–3008, https://doi.org/10.5194/tc-19-2983-2025, 2025.

Gelman, A., Carlin, J. B., Stern, H. S., Dunson, D. B., Vehtari, A., and Rubin, D. B.: Bayesian Data Analysis, Chapman and Hall/CRC, 3 edn., ISBN 978-0-429-11307-9, https://doi.org/10.1201/b16018, 2013.

GeoSphere Austria: Messstationen Stundendaten v2, https://doi.org/10.60669/9BDM-YQ93, 2024.

https://doi.org/10.5194/egusphere-2025-6249
Preprint. Discussion started: 21 January 2026

Giesen, R. H. and Oerlemans, J.: Calibration of a surface mass balance model for global-scale applications, The Cryosphere, 6, 1463–1481, https://doi.org/10.5194/tc-6-1463-2012, 2012.

Goger, B., Stiperski, I., Nicholson, L., and Sauter, T.: Large-eddy simulations of the atmospheric boundary layer over an Alpine glacier: Impact of synoptic flow direction and governing processes, Quarterly Journal of the Royal Meteorological Society, 148, 1319–1343, https://doi.org/10.1002/qj.4263, 2022.

Gorelick, N., Hancher, M., Dixon, M., Ilyushchenko, S., Thau, D., and Moore, R.: Google Earth Engine: Planetary-scale geospatial analysis for everyone, Remote Sensing of Environment, https://doi.org/10.1016/j.rse.2017.06.031, 2017.

Greuell, W., Knap, W. H., and Smeets, P. C.: Elevational changes in meteorological variables along a midlatitude glacier during summer, Journal of Geophysical Research: Atmospheres, 102, 25 941–25 954, https://doi.org/10.1029/97JD02083, 1997.

Gromke, C., Manes, C., Walter, B., Lehning, M., and Guala, M.: Aerodynamic Roughness Length of Fresh Snow, Boundary-Layer Meteorology, 141, 21–34, https://doi.org/10.1007/s10546-011-9623-3, 2011.

Gurgiser, W., Mölg, T., Nicholson, L., and Kaser, G.: Mass-balance model parameter transferability on a tropical glacier, Journal of Glaciology, 59, 845–858, https://doi.org/10.3189/2013JoG12J226, 2013.

Günther, D., Marke, T., Essery, R., and Strasser, U.: Uncertainties in Snowpack Simulations—Assessing the Impact of Model Structure, Parameter Choice, and Forcing Data Error on Point-Scale Energy Balance Snow Model Performance, Water Resources Research, 55, 2779–2800, https://doi.org/10.1029/2018WR023403, 2019.

Haeberli, W., Hoelzle, M., Paul, F., and Zemp, M.: Integrated monitoring of mountain glaciers as key indicators of global climate change: the European Alps, Annals of Glaciology, 46, 150–160, https://doi.org/10.3189/172756407782871512, 2007.

Hantel, M., Ehrendorfer, M., and Haslinger, A.: Climate sensitivity of snow cover duration in Austria, International Journal of Climatology, 20, 615–640, https://doi.org/10.1002/(SICI)1097-0088(200005)20:6<615::AID-JOC489>3.0.CO;2-0, 2000.

Havens, S., Marks, D., FitzGerald, K., Masarik, M., Flores, A. N., Kormos, P., and Hedrick, A.: Approximating Input Data to a Snowmelt Model Using Weather Research and Forecasting Model Outputs in Lieu of Meteorological Measurements, Journal of Hydrometeorology, 20, 847–862, https://doi.org/10.1175/JHM-D-18-0146.1, 2019.

He, C., Chen, F., Barlage, M., Liu, C., Newman, A., Tang, W., Ikeda, K., and Rasmussen, R.: Can Convection-Permitting Modeling Provide Decent Precipitation for Offline High-Resolution Snowpack Simulations Over Mountains?, Journal of Geophysical Research: Atmospheres, 124, 12 631–12 654, https://doi.org/10.1029/2019JD030823, 2019.

Hentgen, L., Ban, N., Kröner, N., Leutwyler, D., and Schär, C.: Clouds in Convection-Resolving Climate Simulations Over Europe, Journal of Geophysical Research: Atmospheres, 124, 3849–3870, https://doi.org/10.1029/2018JD030150, 2019.

Hochreiter, S. and Schmidhuber, J.: Long Short-Term Memory, Neural Computation, 9, 1735–1780, https://doi.org/10.1162/neco.1997.9.8.1735, 1997.

Hock, R.: Temperature index melt modelling in mountain areas, Journal of Hydrology, 282, 104–115, https://doi.org/10.1016/S0022-1694(03)00257-9, 2003.

Hock, R. and Holmgren, B.: A distributed surface energy-balance model for complex topography and its application to Storglaciären, Sweden, Journal of Glaciology, 51, 25–36, https://doi.org/10.3189/172756505781829566, 2005.

Hock, R., Bliss, A., Marzeion, B., Giesen, R. H., Hirabayashi, Y., Huss, M., Radić, V., and Slangen, A. B. A.: GlacierMIP – A model intercomparison of global-scale glacier mass-balance models and projections, Journal of Glaciology, 65, 453–467, https://doi.org/10.1017/jog.2019.22, 2019.

Huang, W., He, X., Yang, Z., Qiu, T., Wright, J. S., Wang, B., and Lin, D.: Moisture Sources for Wintertime Extreme Precipitation Events Over South China During 1979–2013, Journal of Geophysical Research: Atmospheres, 123, 6690–6712, https://doi.org/10.1029/2018JD028485, 2018.

Hugonnet, R., McNabb, R., Berthier, E., Menounos, B., Nuth, C., Girod, L., Farinotti, D., Huss, M., Dussaillant, I., Brun, F., and Kääb, A.: Accelerated global glacier mass loss in the early twenty-first century, Nature, 592, 726–731, https://doi.org/10.1038/s41586-021-03436-z, 2021.

Huintjes, E.: Energy and Mass Balance Modelling for Glaciers on the Tibetan Plateau: Extension, Validation and Application of a Coupled Snow and Energy Balance Model, PhD, RWTH Aachen University, Aachen, https://publications.rwth-aachen.de/record/459462, 2014.

Huss, M.: Density assumptions for converting geodetic glacier volume change to mass change, The Cryosphere, 7, 877–887, https://doi.org/10.5194/tc-7-877-2013, 2013.

Huss, M. and Hock, R.: A new model for global glacier change and sea-level rise, Frontiers in Earth Science, 3, https://doi.org/10.3389/feart.2015.00054, 2015.

Huss, M., Bauder, A., Funk, M., and Hock, R.: Determination of the seasonal mass balance of four Alpine glaciers since 1865, Journal of Geophysical Research: Earth Surface, 113, 2007JF000 803, https://doi.org/10.1029/2007JF000803, 2008.

Ing, R. N., Ely, J. C., Jones, J. M., and Davies, B. J.: Surface mass balance modelling of the Juneau Icefield highlights the potential for rapid ice loss by the mid-21st century, Journal of Glaciology, 71, e11, https://doi.org/10.1017/jog.2024.82, 2025.

Ismail, M. F., Bogacki, W., Disse, M., Schäfer, M., and Kirschbauer, L.: Estimating degree-day factors of snow based on energy flux components, The Cryosphere, 17, 211–231, https://doi.org/10.5194/tc-17-211-2023, 2023.

Jennings, K. S. and Molotch, N. P.: The sensitivity of modeled snow accumulation and melt to precipitation phase methods across a climatic gradient, Hydrology and Earth System Sciences, 23, 3765–3786, https://doi.org/10.5194/hess-23-3765-2019, 2019.

Jennings, K. S., Winchell, T. S., Livneh, B., and Molotch, N. P.: Spatial variation of the rain–snow temperature threshold across the Northern Hemisphere, Nature Communications, 9, 1148, https://doi.org/10.1038/s41467-018-03629-7, 2018.

Jiao, H., Li, G., Chen, Z., and Cheng, X.: Glacier surface melt monitoring using Sentinel-1 SAR backscattering coefficient and polarimetric decomposition features at Greenland ice sheet, Geo-spatial Information Science, pp. 1–23, https://doi.org/10.1080/10095020.2025.2514817, 2025.

Johnson, E. and Rupper, S.: An Examination of Physical Processes That Trigger the Albedo-Feedback on Glacier Surfaces and Implications for Regional Glacier Mass Balance Across High Mountain Asia, Frontiers in Earth Science, 8, 129, https://doi.org/10.3389/feart.2020.00129, 2020.

Khadka, A., Brun, F., Wagnon, P., Shrestha, D., and Sherpa, T. C.: Surface energy and mass balance of Mera Glacier (Nepal, Central Himalaya) and their sensitivity to temperature and precipitation, Journal of Glaciology, pp. 1–22, https://doi.org/10.1017/jog.2024.42, 2024.

Klok, E. L. and Oerlemans, J.: Model study of the spatial distribution of the energy and mass balance of Morteratschgletscher, Switzerland, Journal of Glaciology, 48, 505–518, https://doi.org/10.3189/172756502781831133, 2002.

Klug, C., Bollmann, E., Galos, S. P., Nicholson, L., Prinz, R., Rieg, L., Sailer, R., Stötter, J., and Kaser, G.: Geodetic reanalysis of annual glaciological mass balances (2001–2011) of Hintereisferner, Austria, The Cryosphere, 12, 833–849, https://doi.org/10.5194/tc-12-833-2018, 2018.

Kneib, M., Dehecq, A., Gilbert, A., Basset, A., Miles, E. S., Jouvet, G., Jourdain, B., Ducasse, E., Beraud, L., Rabatel, A., Mouginot, J., Carcanade, G., Laarman, O., Brun, F., and Six, D.: Distributed surface mass balance of an avalanche-fed glacier, The Cryosphere, 18, 5965–5983, https://doi.org/10.5194/tc-18-5965-2024, 2024.

Kochendorfer, J., Rasmussen, R., Wolff, M., Baker, B., Hall, M. E., Meyers, T., Landolt, S., Jachcik, A., Isaksen, K., Brækkan, R., and Leeper, R.: The quantification and correction of wind-induced precipitation measurement errors, Hydrology and Earth System Sciences, 21, 1973–1989, https://doi.org/10.5194/hess-21-1973-2017, 2017.

Konzelmann, T., Vandewal, R., Greuell, W., Bintanja, R., Henneken, E., and Abeouchi, A.: Parameterization of global and longwave incoming radiation for the Greenland Ice Sheet, Global and Planetary Change, 9, 143–164, https://doi.org/10.1016/0921-8181(94)90013-2, 1994.

Kuhn, M., Dreiseitl, E., Hofinger, S., Markl, G., Span, N., and Kaser, G.: Measurements and Models of the Mass Balance of Hintereisferner, Geografiska Annaler, Series A: Physical Geography, 81, 659–670, https://doi.org/10.1111/j.0435-3676.1999.00094.x, 1999.

Landmann, J. M., Künsch, H. R., Huss, M., Ogier, C., Kalisch, M., and Farinotti, D.: Assimilating near-real-time mass balance stake readings into a model ensemble using a particle filter, The Cryosphere, 15, 5017–5040, https://doi.org/10.5194/tc-15-5017-2021, 2021.

Lapo, K. E., Hinkelman, L. M., Raleigh, M. S., and Lundquist, J. D.: Impact of errors in the downwelling irradiances on simulations of snow water equivalent, snow surface temperature, and the snow energy balance, Water Resources Research, 51, 1649–1670, https://doi.org/10.1002/2014WR016259, 2015.

Lecavalier, B. S. and Tarasov, L.: A history-matching analysis of the Antarctic Ice Sheet since the Last Interglacial – Part 1: Ice sheet evolution, The Cryosphere, 19, 919–953, https://doi.org/10.5194/tc-19-919-2025, 2025.

Leutwyler, D., Lüthi, D., Ban, N., Fuhrer, O., and Schär, C.: Evaluation of the convection-resolving climate modeling approach on continental scales, Journal of Geophysical Research: Atmospheres, 122, 5237–5258, https://doi.org/10.1002/2016JD026013, 2017.

Li, P., Furtado, K., Zhou, T., Chen, H., and Li, J.: Convection-permitting modelling improves simulated precipitation over the central and eastern Tibetan Plateau, Quarterly Journal of the Royal Meteorological Society, 147, 341–362, https://doi.org/10.1002/qj.3921, 2021.

Litt, M., Shea, J., Wagnon, P., Steiner, J., Koch, I., Stigter, E., and Immerzeel, W.: Glacier ablation and temperature indexed melt models in the Nepalese Himalaya, Scientific Reports, 9, 5264, https://doi.org/10.1038/s41598-019-41657-5, 2019.

Loibl, D.: MountAiN glacier Transient snowline Retrieval Algorithm (MANTRA), https://doi.org/10.5281/ZENODO.8044734, 2023.

Loibl, D., Richter, N., and Grünberg, I.: Remote sensing-derived time series of transient glacier snowline altitudes for High Mountain Asia, 1985–2021, Scientific Data, 12, 103, https://doi.org/10.1038/s41597-024-04309-6, 2025.

Lundquist, J., Hughes, M., Gutmann, E., and Kapnick, S.: Our Skill in Modeling Mountain Rain and Snow is Bypassing the Skill of Our Observational Networks, Bulletin of the American Meteorological Society, 100, 2473–2490, https://doi.org/10.1175/BAMS-D-19-0001.1, 2019.

Lüthi, S., Ban, N., Kotlarski, S., Steger, C. R., Jonas, T., and Schär, C.: Projections of Alpine Snow-Cover in a High-Resolution Climate Simulation, Atmosphere, 10, 463, https://doi.org/10.3390/atmos10080463, 2019.

Ma, M., Ou, T., Liu, D., Wang, S., Fang, J., and Tang, J.: Summer regional climate simulations over Tibetan Plateau: from gray zone to convection permitting scale, Climate Dynamics, 60, 301–322, https://doi.org/10.1007/s00382-022-06314-0, 2023.

MacDougall, A. H., Wheler, B. A., and Flowers, G. E.: A preliminary assessment of glacier melt-model parameter sensitivity and transferability in a dry subarctic environment, The Cryosphere, 5, 1011–1028, https://doi.org/10.5194/tc-5-1011-2011, 2011.

Mackay, J. D., Barrand, N. E., Hannah, D. M., Potter, E., Montoya, N., and Buytaert, W.: Physically based modelling of glacier evolution under climate change in the tropical Andes, The Cryosphere, 19, 685–712, https://doi.org/10.5194/tc-19-685-2025, 2025.

https://doi.org/10.5194/egusphere-2025-6249
Preprint. Discussion started: 21 January 2026

Marzeion, B., Jarosch, A. H., and Hofer, M.: Past and future sea-level change from the surface mass balance of glaciers, The Cryosphere, 6, 1295–1322, https://doi.org/10.5194/tc-6-1295-2012, 2012.

Marzeion, B., Hock, R., Anderson, B., Bliss, A., Champollion, N., Fujita, K., Huss, M., Immerzeel, W. W., Kraaijenbrink, P., Malles, J., Maussion, F., Radić, V., Rounce, D. R., Sakai, A., Shannon, S., Van De Wal, R., and Zekollari, H.: Partitioning the Uncertainty of Ensemble Projections of Global Glacier Mass Change, Earth's Future, 8, e2019EF001 470, https://doi.org/10.1029/2019EF001470, 2020.

McKay, M. D., Beckman, R. J., and Conover, W. J.: A Comparison of Three Methods for Selecting Values of Input Variables in the Analysis of Output from a Computer Code, Technometrics, 21, 239, https://doi.org/10.2307/1268522, 1979.

Miles, E., McCarthy, M., Dehecq, A., Kneib, M., Fugger, S., and Pellicciotti, F.: Health and sustainability of glaciers in High Mountain Asia, Nature Communications, 12, 2868, https://doi.org/10.1038/s41467-021-23073-4, 2021.

Morlighem, M. and Goldberg, D.: Data Assimilation in Glaciology, in: Applications of Data Assimilation and Inverse Problems in the Earth Sciences, edited by Ismail-Zadeh, A., Castelli, F., Jones, D., and Sanchez, S., pp. 93–111, Cambridge University Press, 1 edn., ISBN 978-1-009-18041-2 978-1-009-18040-5, https://doi.org/10.1017/9781009180412.007, 2023.

Mott, R., Stiperski, I., and Nicholson, L.: Spatio-temporal flow variations driving heat exchange processes at a mountain glacier, The Cryosphere, 14, 4699–4718, https://doi.org/10.5194/tc-14-4699-2020, 2020.

Mott, R., Winstral, A., Cluzet, B., Helbig, N., Magnusson, J., Mazzotti, G., Quéno, L., Schirmer, M., Webster, C., and Jonas, T.: Operational snow-hydrological modeling for Switzerland, Frontiers in Earth Science, 11, 1228 158, https://doi.org/10.3389/feart.2023.1228158, 2023.

Mölg, T. and Kaser, G.: A new approach to resolving climate-cryosphere relations: Downscaling climate dynamics to glacier-scale mass and energy balance without statistical scale linking, Journal of Geophysical Research, 116, D16 101, https://doi.org/10.1029/2011JD015669, 2011.

Mölg, T., Cullen, N. J., Hardy, D. R., Winkler, M., and Kaser, G.: Quantifying Climate Change in the Tropical Midtroposphere over East Africa from Glacier Shrinkage on Kilimanjaro, Journal of Climate, 22, 4162–4181, https://doi.org/10.1175/2009JCLI2954.1, 2009.

Mölg, T., Maussion, F., Yang, W., and Scherer, D.: The footprint of Asian monsoon dynamics in the mass and energy balance of a Tibetan glacier, The Cryosphere, 6, 1445–1461, https://doi.org/10.5194/tc-6-1445-2012, 2012.

Naegeli, K., Huss, M., and Hoelzle, M.: Change detection of bare-ice albedo in the Swiss Alps, The Cryosphere, 13, 397–412, https://doi.org/10.5194/tc-13-397-2019, 2019.

NASA JPL: NASADEM Merged DEM Global 1 arc second V001, https://doi.org/10.5067/MEASURES/NASADEM/NASADEM_HGT.001, 2020.

Nicholson, L., Stiperski, I., Nitti, G., Prinz, R., Georgi, A., Groos, A. R., Shaw, T. E., Sauter, T., Haugeneder, M., Mott, R., Sicart, J.-E., Brock, B. W., Albers, R., Allegri, B., Barral, H., Biron, R., Charrondiere, C., Coulaud, C., Fischer, A., Reynolds, D., Richter, N., Schroeder, M., Vettori, P., Voordendag, A., and Wydra, C.: The second HinterEisFerner EXperiment (HEFEX II): Initial insights into boundary layer structure and surface-atmosphere exchange processes from intensive observations at a valley glacier, Bulletin of the American Meteorological Society, pp. BAMS–D–24–0010.1, https://doi.org/10.1175/BAMS-D-24-0010.1, 2025.

Nicholson, L. I., Prinz, R., Mölg, T., and Kaser, G.: Micrometeorological conditions and surface mass and energy fluxes on Lewis Glacier, Mt Kenya, in relation to other tropical glaciers, The Cryosphere, 7, 1205–1225, https://doi.org/10.5194/tc-7-1205-2013, 2013.

Nie, Y., Pritchard, H. D., Liu, Q., Hennig, T., Wang, W., Wang, X., Liu, S., Nepal, S., Samyn, D., Hewitt, K., and Chen, X.: Glacial change and hydrological implications in the Himalaya and Karakoram, Nature Reviews Earth & Environment, 2, 91–106, https://doi.org/10.1038/s43017-020-00124-w, 2021.

Obleitner, F.: Hintereisferner energy balance data set, https://doi.org/10.5281/ZENODO.6483368, 2022.

https://doi.org/10.5194/egusphere-2025-6249
Preprint. Discussion started: 21 January 2026

Oerlemans, J.: Glaciers and climate change, Balkema, Lisse, ISBN 978-90-265-1813-3, 2001.

Oerlemans, J. and Knap, W. H.: A 1 year record of global radiation and albedo in the ablation zone of Morteratschgletscher, Switzerland, Journal of Glaciology, 44, 231–238, https://doi.org/10.3189/S0022143000002574, 1998.

Oerlemans, J., Giesen, R., and Van Den Broeke, M.: Retreating alpine glaciers: increased melt rates due to accumulation of dust (Vadret da Morteratsch, Switzerland), Journal of Glaciology, 55, 729–736, https://doi.org/10.3189/002214309789470969, 2009.

Ohmura, A.: Physical Basis for the Temperature-Based Melt-Index Method, Journal of Applied Meteorology, 40, 753–761, https://doi.org/10.1175/1520-0450(2001)040<0753:PBFTTB>2.0.CO;2, 2001.

Olefs, M. and Obleitner, F.: Numerical simulations on artificial reduction of snow and ice ablation, Water Resources Research, 43, 2006WR005 065, https://doi.org/10.1029/2006WR005065, 2007.

Prein, A. F. and Gobiet, A.: Impacts of uncertainties in European gridded precipitation observations on regional climate analysis, International Journal of Climatology, 37, 305–327, https://doi.org/10.1002/joc.4706, 2017.

Prinz, R., Nicholson, L. I., Mölg, T., Gurgiser, W., and Kaser, G.: Climatic controls and climate proxy potential of Lewis Glacier, Mt. Kenya, The Cryosphere, 10, 133–148, https://doi.org/10.5194/tc-10-133-2016, 2016.

Quéno, L., Vionnet, V., Dombrowski-Etchevers, I., Lafaysse, M., Dumont, M., and Karbou, F.: Snowpack modelling in the Pyrenees driven by kilometric-resolution meteorological forecasts, The Cryosphere, 10, 1571–1589, https://doi.org/10.5194/tc-10-1571-2016, 2016.

Quéno, L., Mott, R., Morin, P., Cluzet, B., Mazzotti, G., and Jonas, T.: Snow redistribution in an intermediate-complexity snow hydrology modelling framework, The Cryosphere, 18, 3533–3557, https://doi.org/10.5194/tc-18-3533-2024, 2024.

Rabatel, A., Sirguey, P., Drolon, V., Maisongrande, P., Arnaud, Y., Berthier, E., Davaze, L., Dedieu, J.-P., and Dumont, M.: Annual and Seasonal Glacier-Wide Surface Mass Balance Quantified from Changes in Glacier Surface State: A Review on Existing Methods Using Optical Satellite Imagery, Remote Sensing, 9, 507, https://doi.org/10.3390/rs9050507, 2017.

Racoviteanu, A. E., Rittger, K., and Armstrong, R.: An Automated Approach for Estimating Snowline Altitudes in the Karakoram and Eastern Himalaya From Remote Sensing, Frontiers in Earth Science, 7, 220, https://doi.org/10.3389/feart.2019.00220, 2019.

Raleigh, M. S., Lundquist, J. D., and Clark, M. P.: Exploring the impact of forcing error characteristics on physically based snow simulations within a global sensitivity analysis framework, Hydrology and Earth System Sciences, 19, 3153–3179, https://doi.org/10.5194/hess-19-3153-2015, 2015.

Raleigh, M. S., Livneh, B., Lapo, K., and Lundquist, J. D.: How Does Availability of Meteorological Forcing Data Impact Physically Based Snowpack Simulations?*, Journal of Hydrometeorology, 17, 99–120, https://doi.org/10.1175/JHM-D-14-0235.1, 2016.

Rastner, P., Prinz, R., Notarnicola, C., Nicholson, L., Sailer, R., Schwaizer, G., and Paul, F.: On the Automated Mapping of Snow Cover on Glaciers and Calculation of Snow Line Altitudes from Multi-Temporal Landsat Data, Remote Sensing, 11, 1410, https://doi.org/10.3390/rs11121410, 2019.

Ren, S., Miles, E. S., Jia, L., Menenti, M., Kneib, M., Buri, P., McCarthy, M. J., Shaw, T. E., Yang, W., and Pellicciotti, F.: Anisotropy Parameterization Development and Evaluation for Glacier Surface Albedo Retrieval from Satellite Observations, Remote Sensing, 13, 1714, https://doi.org/10.3390/rs13091714, 2021.

Ren, S., Jia, L., Miles, E. S., Menenti, M., Kneib, M., Shaw, T. E., Buri, P., McCarthy, M. J., Yang, W., Pellicciotti, F., and Yao, T.: Observed and projected declines in glacier albedo across the Third Pole in the 21st century, One Earth, 7, 1587–1599, https://doi.org/10.1016/j.oneear.2024.08.010, 2024.

Reynolds, D., Quéno, L., Lehning, M., Jafari, M., Berg, J., Jonas, T., Haugeneder, M., and Mott, R.: Seasonal snow–atmosphere modeling: let's do it, The Cryosphere, 18, 4315–4333, https://doi.org/10.5194/tc-18-4315-2024, 2024.

https://doi.org/10.5194/egusphere-2025-6249
Preprint. Discussion started: 21 January 2026

Reynolds, D. S., Gutmann, E., Kruyt, B., Haugeneder, M., Jonas, T., Gerber, F., Lehning, M., and Mott, R.: The High-resolution Intermediate Complexity Atmospheric Research (HICAR v1.0) Model Enables Fast Dynamic Downscaling to the Hectometer Scale, https://doi.org/10.5194/gmd-2023-16, 2023.

RGI Consortium: Randolph Glacier Inventory - A Dataset of Global Glacier Outlines, Version 6, https://doi.org/10.7265/4M1F-GD79, 2017.

Richter, N.: Scripts used for the preparation of the manuscript titled "Towards the Bayesian calibration of a glacier surface energy balance model for unmonitored glaciers", https://doi.org/10.5281/ZENODO.17426864, 2025.

Rockel, B., Will, A., and Hense, A.: The Regional Climate Model COSMO?CLM (CCLM), Meteorologische Zeitschrift, 17, 347–348, https://doi.org/10.1127/0941?2948/2008/0309, place: Stuttgart, Germany Publisher: Schweizerbart Science Publishers, 2008.

Roe, G., Baker, M., and Herla, F.: Centennial glacier retreat as categorical evidence of regional climate change, Nature Geoscience, 10, 95–99, https://doi.org/10.1038/ngeo2863, 2017.

Rounce, D. R., Khurana, T., Short, M. B., Hock, R., Shean, D. E., and Brinkerhoff, D. J.: Quantifying parameter uncertainty in a large-scale glacier evolution model using Bayesian inference: application to High Mountain Asia, Journal of Glaciology, 66, 175–187, https://doi.org/10.1017/jog.2019.91, 2020.

Rounce, D. R., Hock, R., Maussion, F., Hugonnet, R., Kochtitzky, W., Huss, M., Berthier, E., Brinkerhoff, D., Compagno, L., Copland, L., Farinotti, D., Menounos, B., and McNabb, R. W.: Global glacier change in the 21st century: Every increase in temperature matters, Science, 379, 78–83, https://doi.org/10.1126/science.abo1324, 2023.

Rumelhart, D. E., Hinton, G. E., and Williams, R. J.: Learning representations by back-propagating errors, Nature, 323, 533–536, https://doi.org/10.1038/323533a0, 1986.

Rye, C. J., Willis, I. C., Arnold, N. S., and Kohler, J.: On the need for automated multiobjective optimization and uncertainty estimation of glacier mass balance models, Journal of Geophysical Research: Earth Surface, 117, 2011JF002 184, https://doi.org/10.1029/2011JF002184, 2012.

Réveillet, M., Six, D., Vincent, C., Rabatel, A., Dumont, M., Lafaysse, M., Morin, S., Vionnet, V., and Litt, M.: Relative performance of empirical and physical models in assessing the seasonal and annual glacier surface mass balance of Saint-Sorlin Glacier (French Alps), The Cryosphere, 12, 1367–1386, https://doi.org/10.5194/tc-12-1367-2018, 2018.

Saigger, M., Sauter, T., Schmid, C., Collier, E., Goger, B., Kaser, G., Prinz, R., Voordendag, A., and Mölg, T.: A Drifting and Blowing Snow Scheme in the Weather Research and Forecasting Model, Journal of Advances in Modeling Earth Systems, 16, e2023MS004 007, https://doi.org/10.1029/2023MS004007, 2024.

Sakai, A. and Fujita, K.: Contrasting glacier responses to recent climate change in high-mountain Asia, Scientific Reports, 7, 13 717, https://doi.org/10.1038/s41598-017-14256-5, 2017.

Sauter, T. and Obleitner, F.: Assessing the uncertainty of glacier mass-balance simulations in the European Arctic based on variance decomposition, Geoscientific Model Development, 8, 3911–3928, https://doi.org/10.5194/gmd-8-3911-2015, publisher: Copernicus GmbH, 2015.

Sauter, T., Arndt, A., and Schneider, C.: COSIPY v1.3 – an open-source coupled snowpack and ice surface energy and mass balance model, Geoscientific Model Development, 13, 5645–5662, https://doi.org/10.5194/gmd-13-5645-2020, 2020.

Scher, C., Steiner, N. C., and McDonald, K. C.: Mapping seasonal glacier melt across the Hindu Kush Himalaya with time series synthetic aperture radar (SAR), The Cryosphere, 15, 4465–4482, https://doi.org/10.5194/tc-15-4465-2021, 2021.

Schrott, D.: Flächenhafte Modellierung der Energie- und Massenbilanz am Hintereisferner: das Haushaltsjahr 2003/04, Diplomarbeit, Universität Innsbruck, https://fileshare.uibk.ac.at/d/fdd6210c9e9b4b1eba11/files/?p=%2Fschrott_daniel_2006_dipl.pdf, 2006.

Schuster, L., Rounce, D. R., and Maussion, F.: Glacier projections sensitivity to temperature-index model choices and calibration strategies, Annals of Glaciology, pp. 1–16, https://doi.org/10.1017/aog.2023.57, 2023.

Schuster, M. and Paliwal, K.: Bidirectional recurrent neural networks, IEEE Transactions on Signal Processing, 45, 2673–2681, https://doi.org/10.1109/78.650093, 1997.

Schär, C., Vidale, P. L., Lüthi, D., Frei, C., Häberli, C., Liniger, M. A., and Appenzeller, C.: The role of increasing temperature variability in European summer heatwaves, Nature, 427, 332–336, https://doi.org/10.1038/nature02300, 2004.

Shannon, S., Smith, R., Wiltshire, A., Payne, T., Huss, M., Betts, R., Caesar, J., Koutroulis, A., Jones, D., and Harrison, S.: Global glacier volume projections under high-end climate change scenarios, The Cryosphere, 13, 325–350, https://doi.org/10.5194/tc-13-325-2019, 2019.

Shaw, T., Jouberton, A., Niwano, M., Kneib, M., Fujita, K., and Pellicciotti, F.: Precipitation Uncertainty Hampers the Understanding of Glacier Response in High Mountain Asia, https://doi.org/10.5194/egusphere-egu25-6679, 2025.

Shugar, D. H., Jacquemart, M., Shean, D., Bhushan, S., Upadhyay, K., Sattar, A., Schwanghart, W., McBride, S., De Vries, M. V. W., Mergili, M., Emmer, A., Deschamps-Berger, C., McDonnell, M., Bhambri, R., Allen, S., Berthier, E., Carrivick, J. L., Clague, J. J., Dokukin, M., Dunning, S. A., Frey, H., Gascoin, S., Haritashya, U. K., Huggel, C., Kääb, A., Kargel, J. S., Kavanaugh, J. L., Lacroix, P., Petley, D., Rupper, S., Azam, M. F., Cook, S. J., Dimri, A. P., Eriksson, M., Farinotti, D., Fiddes, J., Gnyawali, K. R., Harrison, S., Jha, M., Koppes, M., Kumar, A., Leinss, S., Majeed, U., Mal, S., Muhuri, A., Noetzli, J., Paul, F., Rashid, I., Sain, K., Steiner, J., Ugalde, F., Watson, C. S., and Westoby, M. J.: A massive rock and ice avalanche caused the 2021 disaster at Chamoli, Indian Himalaya, Science, 373, 300–306, https://doi.org/10.1126/science.abh4455, 2021.

Sicart, J. E., Hock, R., and Six, D.: Glacier melt, air temperature, and energy balance in different climates: The Bolivian Tropics, the French Alps, and northern Sweden, Journal of Geophysical Research: Atmospheres, 113, 2008JD010 406, https://doi.org/10.1029/2008JD010406, 2008.

Silwal, G., Ammar, M. E., Thapa, A., Bonsal, B., and Faramarzi, M.: Response of glacier modelling parameters to time, space, and model complexity: Examples from eastern slopes of Canadian Rocky Mountains, Science of The Total Environment, 872, 162 156, https://doi.org/10.1016/j.scitotenv.2023.162156, 2023.

Sirguey, P., Still, H., Cullen, N. J., Dumont, M., Arnaud, Y., and Conway, J. P.: Reconstructing the mass balance of Brewster Glacier, New Zealand, usingMODIS-derived glacier-wide albedo, The Cryosphere, 10, 2465–2484, https://doi.org/10.5194/tc-10-2465-2016, 2016.

Sjursen, K. H., Dunse, T., Tambue, A., Schuler, T. V., and Andreassen, L. M.: Bayesian parameter estimation in glacier mass-balance modelling using observations with distinct temporal resolutions and uncertainties, Journal of Glaciology, pp. 1–20, https://doi.org/10.1017/jog.2023.62, 2023.

Sjursen, K. H., Dunse, T., Schuler, T. V., Andreassen, L. M., and Åkesson, H.: Spatiotemporal mass-balance variability of Jostedalsbreen Ice Cap, Norway, revealed by a temperature-index model using Bayesian inference, Annals of Glaciology, 66, e1, https://doi.org/10.1017/aog.2024.41, 2025.

Slater, A. G., Schlosser, C. A., Desborough, C. E., Pitman, A. J., Henderson-Sellers, A., Robock, A., Vinnikov, K. Y., Entin, J., Mitchell, K., Chen, F., Boone, A., Etchevers, P., Habets, F., Noilhan, J., Braden, H., Cox, P. M., De Rosnay, P., Dickinson, R. E., Yang, Z.-L., Dai, Y.-J., Zeng, Q., Duan, Q., Koren, V., Schaake, S., Gedney, N., Gusev, Y. M., Nasonova, O. N., Kim, J., Kowalczyk, E. A., Shmakin, A. B., Smirnova, T. G., Verseghy, D., Wetzel, P., and Xue, Y.: The Representation of Snow in Land Surface Schemes: Results from PILPS 2(d), Journal of Hydrometeorology, 2, 7–25, https://doi.org/10.1175/1525-7541(2001)002<0007:TROSIL>2.0.CO;2, 2001.

Smith, T., Smith, M. W., Chambers, J. R., Sailer, R., Nicholson, L., Mertes, J., Quincey, D. J., Carrivick, J. L., and Stiperski, I.: A scale-dependent model to represent changing aerodynamic roughness of ablating glacier ice based on repeat topographic surveys, Journal of Glaciology, 66, 950–964, https://doi.org/10.1017/jog.2020.56, 2020.

Steger, C. R., Steger, B., and Schär, C.: HORAYZON v1.2: an efficient and flexible ray-tracing algorithm to compute horizon and sky view factor, Geoscientific Model Development, 15, 6817–6840, https://doi.org/10.5194/gmd-15-6817-2022, 2022.

Strasser, U., Marke, T., Braun, L., Escher-Vetter, H., Juen, I., Kuhn, M., Maussion, F., Mayer, C., Nicholson, L., Niedertscheider, K., Sailer, R., Stötter, J., Weber, M., and Kaser, G.: The Rofental: a high Alpine research basin (1890–3770 m a.s.l.) in the Ötztal Alps (Austria) with over 150 years of hydrometeorological and glaciological observations, Earth System Science Data, 10, 151–171, https://doi.org/10.5194/essd-10-151-2018, 2018.

Temme, F., Farías-Barahona, D., Seehaus, T., Jaña, R., Arigony-Neto, J., Gonzalez, I., Arndt, A., Sauter, T., Schneider, C., and Fürst, J. J.: Strategies for regional modeling of surface mass balance at the Monte Sarmiento Massif, Tierra del Fuego, The Cryosphere, 17, 2343–2365, https://doi.org/10.5194/tc-17-2343-2023, 2023.

The GlaMBIE Team, Zemp, M., Jakob, L., Dussaillant, I., Nussbaumer, S. U., Gourmelen, N., Dubber, S., A, G., Abdullahi, S., Andreassen, L. M., Berthier, E., Bhattacharya, A., Blazquez, A., Boehm Vock, L. F., Bolch, T., Box, J., Braun, M. H., Brun, F., Cicero, E., Colgan, W., Eckert, N., Farinotti, D., Florentine, C., Floricioiu, D., Gardner, A., Harig, C., Hassan, J., Hugonnet, R., Huss, M., Jóhannesson, T., Liang, C.-C. A., Ke, C.-Q., Khan, S. A., King, O., Kneib, M., Krieger, L., Maussion, F., Mattea, E., McNabb, R., Menounos, B., Miles, E., Moholdt, G., Nilsson, J., Pálsson, F., Pfeffer, J., Piermattei, L., Plummer, S., Richter, A., Sasgen, I., Schuster, L., Seehaus, T., Shen, X., Sommer, C., Sutterley, T., Treichler, D., Velicogna, I., Wouters, B., Zekollari, H., and Zheng, W.: Community estimate of global glacier mass changes from 2000 to 2023, Nature, 639, 382–388, https://doi.org/10.1038/s41586-024-08545-z, 2025.

Ultee, L., Coats, S., and Mackay, J.: Glacial runoff buffers droughts through the 21st century, Earth System Dynamics, 13, 935–959, https://doi.org/10.5194/esd-13-935-2022, 2022.

Van De Wal, R. S. W., Oerlemans, J., and Van Der Hage, J. C.: A study of ablation variations on the tongue of Hintereisferner, Austrian Alps, Journal of Glaciology, 38, 319–324, https://doi.org/10.3189/S0022143000002203, 1992.

Van Tiggelen, M., Smeets, P. C. J. P., Reijmer, C. H., Van As, D., Box, J. E., Fausto, R. S., Khan, S. A., Rignot, E., and Van Den Broeke, M. R.: Surface energy balance closure over melting snow and ice from in situ measurements on the Greenland ice sheet, Journal of Glaciology, 70, e82, https://doi.org/10.1017/jog.2024.68, 2024.

Vionnet, V., Brun, E., Morin, S., Boone, A., Faroux, S., Le Moigne, P., Martin, E., and Willemet, J.-M.: The detailed snowpack scheme Crocus and its implementation in SURFEX v7.2, Geoscientific Model Development, 5, 773–791, https://doi.org/10.5194/gmd-5-773-2012, 2012.

Vionnet, V., Dombrowski-Etchevers, I., Lafaysse, M., Quéno, L., Seity, Y., and Bazile, E.: Numerical Weather Forecasts at Kilometer Scale in the French Alps: Evaluation and Application for Snowpack Modeling, Journal of Hydrometeorology, 17, 2591–2614, https://doi.org/10.1175/JHM-D-15-0241.1, 2016.

Vionnet, V., Six, D., Auger, L., Dumont, M., Lafaysse, M., Quéno, L., Réveillet, M., Dombrowski-Etchevers, I., Thibert, E., and Vincent, C.: Sub-kilometer Precipitation Datasets for Snowpack and Glacier Modeling in Alpine Terrain, Frontiers in Earth Science, 7, 182, https://doi.org/10.3389/feart.2019.00182, 2019.

Vionnet, V., Verville, M., Fortin, V., Brugman, M., Abrahamowicz, M., Lemay, F., Thériault, J. M., Lafaysse, M., and Milbrandt, J. A.: Snow Level From Post-Processing of Atmospheric Model Improves Snowfall Estimate and Snowpack Prediction in Mountains, Water Resources Research, 58, e2021WR031 778, https://doi.org/10.1029/2021WR031778, 2022.

https://doi.org/10.5194/egusphere-2025-6249
Preprint. Discussion started: 21 January 2026

Voordendag, A., Prinz, R., Schuster, L., and Kaser, G.: Brief communication: The Glacier Loss Day as an indicator of a record-breaking negative glacier mass balance in 2022, The Cryosphere, 17, 3661–3665, https://doi.org/10.5194/tc-17-3661-2023, 2023.

Voordendag, A., Goger, B., Prinz, R., Sauter, T., Mölg, T., Saigger, M., and Kaser, G.: A novel framework to investigate wind-driven snow redistribution over an Alpine glacier: combination of high-resolution terrestrial laser scans and large-eddy simulations, The Cryosphere, 18, 849–868, https://doi.org/10.5194/tc-18-849-2024, 2024.

WGMS: Fluctuations of Glaciers Database, https://doi.org/10.5904/WGMS-FOG-2024-01, artwork Size: 684 MB Pages: 684 MB, 2024.

Williamson, S. N., Copland, L., Thomson, L., and Burgess, D.: Comparing simple albedo scaling methods for estimating Arctic glacier mass balance, Remote Sensing of Environment, 246, 111 858, https://doi.org/10.1016/j.rse.2020.111858, 2020.

Zekollari, H., Huss, M., Schuster, L., Maussion, F., Rounce, D. R., Aguayo, R., Champollion, N., Compagno, L., Hugonnet, R., Marzeion, B., Mojtabavi, S., and Farinotti, D.: Twenty-first century global glacier evolution under CMIP6 scenarios and the role of glacier-specific observations, The Cryosphere, 18, 5045–5066, https://doi.org/10.5194/tc-18-5045-2024, 2024.

Zekollari, H., Schuster, L., Maussion, F., Hock, R., Marzeion, B., Rounce, D. R., Compagno, L., Fujita, K., Huss, M., James, M., Kraaijenbrink, P. D. A., Lipscomb, W. H., Minallah, S., Oberrauch, M., Van Tricht, L., Champollion, N., Edwards, T., Farinotti, D., Immerzeel, W., Leguy, G., and Sakai, A.: Glacier preservation doubled by limiting warming to 1.5°C versus 2.7°C, Science, 388, 979–983, https://doi.org/10.1126/science.adu4675, 2025.

Zemp, M., Frey, H., Gärtner-Roer, I., Nussbaumer, S. U., Hoelzle, M., Paul, F., Haeberli, W., Denzinger, F., Ahlstrøm, A. P., Anderson, B., Bajracharya, S., Baroni, C., Braun, L. N., Cáceres, B. E., Casassa, G., Cobos, G., Dávila, L. R., Delgado Granados, H., Demuth, M. N., Espizua, L., Fischer, A., Fujita, K., Gadek, B., Ghazanfar, A., Ove Hagen, J., Holmlund, P., Karimi, N., Li, Z., Pelto, M., Pitte, P., Popovnin, V. V., Portocarrero, C. A., Prinz, R., Sangewar, C. V., Severskiy, I., Sigurđsson, O., Soruco, A., Usubaliev, R., and Vincent, C.: Historically unprecedented global glacier decline in the early 21st century, Journal of Glaciology, 61, 745–762, https://doi.org/10.3189/2015JoG15J017, 2015.

Zemp, M., Huss, M., Thibert, E., Eckert, N., McNabb, R., Huber, J., Barandun, M., Machguth, H., Nussbaumer, S. U., Gärtner-Roer, I., Thomson, L., Paul, F., Maussion, F., Kutuzov, S., and Cogley, J. G.: Global glacier mass changes and their contributions to sea-level rise from 1961 to 2016, Nature, 568, 382–386, https://doi.org/10.1038/s41586-019-1071-0, 2019.

Zhang, Y., Gao, T., Kang, S., Shangguan, D., and Luo, X.: Albedo reduction as an important driver for glacier melting in Tibetan Plateau and its surrounding areas, Earth-Science Reviews, 220, 103 735, https://doi.org/10.1016/j.earscirev.2021.103735, 2021.

Zhu, Y., Liu, S., Brock, B. W., Tian, L., Yi, Y., Xie, F., Shangguan, D., and Shen, Y.: Debris cover effects on energy and mass balance of Batura Glacier in the Karakoram over the past 20 years, Hydrology and Earth System Sciences, 28, 2023–2045, https://doi.org/10.5194/hess-28-2023-2024, 2024.

Zolles, T. and Born, A.: Sensitivity of the Greenland surface mass and energy balance to uncertainties in key model parameters, The Cryosphere, 15, 2917–2938, https://doi.org/10.5194/tc-15-2917-2021, publisher: Copernicus GmbH, 2021.

Zolles, T., Maussion, F., Galos, S. P., Gurgiser, W., and Nicholson, L.: Robust uncertainty assessment of the spatio-temporal transferability of glacier mass and energy balance models, The Cryosphere, 13, 469–489, https://doi.org/10.5194/tc-13-469-2019, 2019.